Supporting Information for

Expiratory aerosol pH: the overlooked driver of airborne virus inactivation

Beiping Luo[1,†], Aline Schaub[2,†], Irina Glas[3,†], Liviana K. Klein[1,†], Shannon C. David[2], Nir Bluvshtein[1], Kalliopi Violaki[4], Ghislain Motos[4], Marie O. Pohl[3], Walter Hugentobler[4], Athanasios Nenes[4,5], Ulrich K. Krieger[1], Silke Stertz[3], Thomas Peter[1,*], and Tamar Kohn[2,*]

[†]these authors contributed equally to this work
[*]Correspondence to: tamar.kohn@epfl.ch and thomas.peter@env.ethz.ch

This PDF file includes:
47 pages
Supporting Methods
Supporting Text
Figures S1 to S20
Tables S1 to S4

Supporting Methods

Virus propagation, purification and enumeration

Influenza virus strain A/WSN/33 (H1N1) was propagated in Madin-Darby Canine Kidney (MDCK) cells (ThermoFisher) and the coronavirus strain HCoV-229E-Ren (kindly provided by Volker Thiel, University of Bern)(1) was propagated in Huh-7cells (a kind gift from Mirco Schmolke, University of Geneva). SARS-CoV-2 strain BetaCoV/Germany/BavPat1/2020 was obtained from the European Virus Archive GLOBAL (EVA-GLOBAL; Ref-SKU: 026V-03883)(2) and propagated in VeroE6 cells (kindly provided by Volker Thiel, University of Bern). All work with infectious SARS-CoV-2 was performed in an approved biosafety level 3 (BSL3) facility by trained personnel at the Institute of Medical Virology, University of Zurich. All procedures and protective measures were thoroughly risk assessed prior to starting the project and were approved by the Swiss Federal Office of Public Health (Ecogen number A202808/3). The cells are maintained in Dulbecco's modified Eagle's medium (DMEM; Gibco) supplemented with 10% Fetal Bovine Serum (FBS; Gibco) and 1% Penicillin-Streptomycin 10,000 U/ml (P/S; Gibco). MDCK, VeroE6 or Huh-7 cell cultures were inoculated with IAV, SARS-CoV-2 or HCoV-229E at a multiplicity of infection of 0.001, 0.001 and 0.01, respectively, for 72 h. Culture supernatants were clarified by centrifugation at 2,500 × g for 10 min, and IAV and HCoV-229E were pelleted through a 30% sucrose cushion at 112,400 × g in a SW32Ti rotor (Beckman) or a AH-629 rotor (ThermoFisher Scientific) for 90 minutes at 4°C. Pellets were recovered in phosphate-buffered saline (PBS) overnight. SARS-CoV-2 stocks were concentrated using Amicon Ultra-15, PLHK Ultracel-PL Membran, 100 kDa tubes (Millipore). The quantification of IAV, SARS-CoV-2 and HCoV-229E titers were done by standard plaque assay on MDCK, VeroE6 or Huh-7 cells respectively with an assay limit of detection (LoD) of 10 PFU/ml. A live-cell Renilla luciferase assay was used as an alternative quantification method to determine HCoV-229E titers in a high-throughput manner. The assay was performed as previously reported (3), on Huh-7 cells at 33°C using 6 µM of the Renilla luciferase substrate EnduRen (Promega) and had an LoD of approximately 500 PFU/ml. Relative Light units were measured at regular intervals with the EnVision multilabel plate reader (PerkinElmer) and the areas under the curve (AUC) were determined. The system was calibrated using reference samples with known titers. All calculations were performed in GraphPad Prism 9.232.

Matrix preparation

Experiments were conducted in aqueous buffer and in two matrices representative of respiratory liquids: synthetic lung fluid (SLF) and nasal mucus. Aqueous buffer was prepared from 0.1 M citric acid (Acros Organics) and 0.2 M disodium phosphate (Fluka), mixed at varying proportions to obtain the targeted pH. The pH of each buffer was verified using a pH meter (Orion™Versa Star Pro™; ThermoFisher Scientific). SLF was prepared as described by Bicer (4), except that immunoglobulin G was omitted (Supp. Table S1). Hank's Balanced Salt Solution (HBSS) without phenol red, lyophilized albumin from human serum, human transferrin, 1,2-dipalmitoyl-sn-glycero-3-phosphocholine (DPPC), 1,2-dipalmitoyl-sn-glycero-3-phospho-rac-(1-glycerol) ammonium salt (DPPG), cholesterol, L-ascorbic acid, uric acid and glutathione were purchased from Sigma Aldrich. Liquid SLF was freeze-dried according to the method described by Hassoun *et al.* (5). To create SLF solutions of different enrichments (1×, 10× or 18×), SLF powder was resuspended in the corresponding volume of milli-Q water and was then acidified to the desired pH with 10% of 10× citric acid-phosphate buffer. Note that SLF enrichments beyond 18× were not experimentally feasible.Nasal mucus was prepared from Nasal Epithelial Cells (NEpCs) from three donors, a 73-year-old male, a 50-year-old male and a 41-year-old female (Epithelix, Switzerland, # EP51AB). Cells

were cultured in airway epithelium basal growth medium (Promocell) containing 10 µM Y-27632 (Tocris) and the according airway growth medium supplement pack (Promocell). The health and differentiation process of NEpCs into air-liquid interface (ALI) cultures were monitored by measuring the transepithelial electrical resistance and performing immunofluorescence as previously described (6). Mucus was harvested every 2 weeks by incubating NEpC ALI cultures on 24-mm PET filter inserts (Sarstedt) with 500 µl of milli-Q water at 37°C for 10 min and collecting the wash. Mucus from the 3 different NEpC donors was combined and stored at -80°C. For inactivation experiments, mucus was thawed and acidified to the desired pH with 10% of 10x citric acid-phosphate buffer.

Measurement of virus aggregate sizes by Dynamic Light Scattering (DLS)

To measure the extent of virus aggregation, IAV was spiked into pH 5 or pH 7 citric acid-phosphate buffer, at a final concentration of 10^{10} PFU/mL. The mean hydrodynamic diameter of viral particles in solution was automatically measured every 2 minutes by DLS using a Zetasizer Nano ZS light scattering instrument (Malvern Panalytical), for a total of 30 minutes. Additionally, samples at pH 5 were neutralized in the cuvette by addition of 2 M Na_2HPO_4 at $t = 30$ min, and rapidly mixed by pipetting. The mean hydrodynamic diameter was automatically measured every 2 min for an additional 60 min. Each buffer alone (no virus) was also measured for 10 min each with no particles detected above 10 µm. All data were analyzed using Zetasizer Software 8.01.4906 (Malvern Panalytical).

SLF characterization by (cryo-)transmission electron microscopy and DLS

Transmission electron microscopy (TEM) was conducted using 15 µl of freshly prepared SLF incubated for 2 minutes on a glow-discharged carbon-coated copper grid (400 mesh). After incubation the grid was washed with solution containing only HBSS (Table S1) and stained with uranyl acetate 2% for 30 seconds. Observations were made using a Tecnai F20 electron microscope (Thermo Fisher, Hillsboro, USA) operated at 200 kV. Digital images were collected using a direct detector camera Falcon III (Thermo Fisher, Hillsboro, USA) 4098 X 4098 pixels using a defocus range between -1.5 µm and -2.5 µm. The characterization of SLF by cryo-transmission electron microscopy (cryo-TEM) was performed using 5 µl of freshly prepared SLF, which was applied onto lacey carbon film grids (300 microMesh, EMS). The grid was blotted in an automatic plunge freezing apparatus (Thermo Fisher, Hillsboro, USA) to control humidity and temperature. Observation was made at -170° C on the Tecnai F20 electron microscope, operated at 200 kV and equipped with a cryo-specimen holder Gatan 626 (Warrendale, PA, USA). Digital images were drift corrected using the camera Falcon III (Thermo Fisher, Hillsboro, USA) 4096 X 4096 pixels. The diameter of the particles in SLF solution was measured by DLS after mixing by vortex for 2 min.

EDB measurements of aerosol thermodynamics and diffusion kinetics

We used an electrodynamic balance (EDB) to measure the thermodynamic and kinetic properties of micrometer-sized SLF and nasal mucus particles under controlled conditions in the gas phase. The EDB is also called particle "trap", as it stabilizes (or traps) a slightly charged particle by electric fields in contact-free levitation. Therefore, it enables to investigate droplets, which are highly supersaturated with respect to precipitation of NaCl and other salts. These supersaturated states (see, e.g., efflorescence-deliquescence hysteresis in Fig. S5) occur regularly during exhalation, but are inaccessible for macroscopic measurements, because the contact with bulk containment walls readily leads to precipitation. Thermodynamic properties such as the particle water content in equilibrium with the gas phase are measured under constant or only very slowly changing conditions in the gas phase. In contrast, rapid changes, as those following crystal nucleation and subsequent efflorescence,

enable the EDB to also determine the kinetics of fast crystal growth and diffusion processes inside a trapped particle.

The EDB consists of two hyperboloidal endcap electrodes and a central ring electrode with an AC field that stabilizes the particle horizontally, and a charged single particle is held at the null point of the balance by a DC field established across the endcaps (7). As we described previously (8, 9), we use the EDB to measure the relative changes in mass and radius of a single levitated particle caused by changes in RH with very high precision. In brief, using a droplet-on-demand generator a charged particle of SLF (2.5× recipe concentrations) or of freshly thawed nasal mucus was injected into the temperature-regulated (15°C) and RH-controlled gas flow in the EDB and levitated by the adjustable DC electric field. The particle experiences three forces along the symmetry axis of the EDB, which balance each other:

$$F_{\mathrm{el}} = F_g + F_{\mathrm{drag}}. \qquad [S1]$$

These are the gravitational force

$$F_g = mg \qquad [S2]$$

and the Stokes drag force

$$F_{\mathrm{drag}} = 6\pi\eta R v_{\mathrm{gas}} \qquad [S3]$$

induced by the downward-oriented gas flow. Here, m denotes the mass, g the gravitational acceleration, η the dynamic viscosity of the gas, R the particle radius and v the velocity of the humidified N_2 gas flow through the EDB. These two forces are balanced by an electrical force, F_{el}, required to maintain the particle in the center of the trap,

$$F_{\mathrm{el}} = \frac{CqU_{\mathrm{DC}}}{2z}, \qquad [S4]$$

where $2z$ is the minimum distance between the endcap electrodes, U_{DC} is the DC voltage between the electrodes, q is the charge on the particle, and C denotes a geometrical constant of the balance. Via Eq. S2, U_{DC} depends on the particle mass with a sensitivity to variations caused by loss or uptake of water vapor in the range of 10^{-13} to 10^{-12} g.

Close to thermodynamic equilibrium, the partitioning of H_2O between the gas and the condensed phase was examined by slowly (within hours to days) cycling RH in the EDB between dry ($<$ 5%) and humid (ca. 90%) conditions. The total N_2 flow was set to 20 sccm (controlled by mass flow controllers). The RH was measured with a capacitance sensor (Sensirion SHT85), which was calibrated by observing the deliquescence of various salts. Its accuracy is estimated to be ±1.5%. In addition, we measured the RH at the inlet and outlet of the environmental chamber with capacitance sensors which were at room temperature. We ensured that the ramps were slow enough that all three sensors showed the same kinetic response to RH change. Thus, the sensor and the particle were exposed to the same RH at all times.

To calibrate mass changes of trapped particles (or equivalently, their mass fraction of solutes), the particles were exposed to dry conditions (i.e., without H_2O exchange with the gas phase) to obtain the voltage corresponding solely to the gravitational force and the drag force at various flows. The voltage contributions due to gravity (U_0) and drag ($U_{\mathrm{drag}}(0)$) were determined from linear regression

of the measured voltage (U_m) at various flows under dry conditions. Next, the force balance equation S1 was rearranged to obtain:

$$U_{\mathrm{corr}}(RH) = U_m(RH) - U_{\mathrm{drag}}(0) \cdot \left(\frac{U_{\mathrm{corr}}(RH)}{U_0} \right)^{\frac{1}{3}}. \qquad [S5]$$

Equation S5 was then analytically solved to retrieve the drag-independent voltage ($U_{\mathrm{corr}}(RH)$). Therefore, at any RH, the mass fraction of solutes is given by $U_0/U_{\mathrm{corr}}(RH)$. It was previously shown that certain particle components may induce slow charge loss (10) over a period of hours to days. To correct for that, measurements under similar condition that demonstrated a difference of at least 1 V from cycle to cycle were linearly adjusted prior to the drag force correction.

To complete the analysis of particle composition, the relative change in radius was determined from relative changes in the wavelength of Mie resonances apparent in continuously recorded broad-band backscattering spectra (9, 11, 12) using the Chylek approximation (13). We first estimated the particle radius at 91% RH. Assuming a constant density and refractive index, we then obtained the radii at all other RH (9). This allows a highly accurate determination of particle radii, but we performed this evaluation only on a subset of our measurements, as the method relies on the particles being spherical (which is only approximately true for the inhomogeneous particles of interest in the present work).

Further ResAM details I: vapor pressures, activity coefficients and pH value

ResAM is a fully Lagrangian model, i.e. shell thicknesses are allowed to change while the number of shells stays constant. Like this, the number of molecules of each species is very well conserved within each shell, changing only due to diffusion between the shells, uptake from the gas phase into the outermost shell, and loss due to salt efflorescence close to the center of the particle. In contrast, fixing the radius of the shells and varying the number of shells with time (Eulerian modeling) may lead to numerical problems. Already small variations in concentrations may then lead to unrealistic, numerically produced pH changes. The Lagrangian ResAM does not have this problem.

Species treated by ResAM

The calculation of composition and pH in the liquid phase of expiratory particles requires knowledge of the vapor pressures of the volatile species and the activities of all species. The particles are highly diluted at the moment of exhalation, but H_2O evaporates rapidly when mixed with dry ambient air. Besides water, the following semi-volatile species, which are important for the pH of exhaled aerosol particles, are considered by ResAM in the exchange with the gas phase: NH_3, HNO_3, HCl, CO_2 and CH_3COOH. In the aqueous phase, ResAM treats the following neutral species: H_2O, organics (with two representatives, one of proteins and one of lipids, see below), NH_3, CO_2, CH_3COOH and NH_4CH_3COO. Acids, bases, as well as water can dissociate in the aqueous solution, and the degree of dissociation determines the concentrations of ions, and thus the pH value. To this end ResAM treats the cations H^+, Na^+, NH_4^+, and the anions OH^-, Cl^-, NO_3^-, HCO_3^-, CO_3^{2-}, and CH_3COO^-. Other minor inorganic species in SLF (see Table S1), such as the anions Ca^{2+}, Mg^{2+} and K^+, are not explicitly treated, but are subsumed under NaCl with the same activity coefficient as the Na^+ ion. This simplification only slightly affects the mass fraction of solutes, the size of the particles, and the computed pH.

We group the organic species in SLF into two classes of different mass, chosen such that the thermodynamic properties measured in the EDB are reproduced. The organics are treated as ideal

components in the fluid (unity activity coefficients), but they affect the physicochemical properties of the fluid via Raoult's law. The first class represents proteins with high molar mass and the second class lipids and antioxidants. The molar masses of these two organic classes are determined by fitting ResAM to the EDB measurements (see Figs. 2 and S9). Effective molar masses of 1000 Da and 190 Da provide the best agreement with the EDB experiments. We note that these masses are smaller than masses of proteins, lipids and antioxidants, respectively, which is likely due to treating these compounds as ideal components in the fluid (future work may explore the non-ideal character of these organic species).

Aerosol initial conditions

The initial properties of freshly formed exhalation aerosol particles have some influence on their readiness to take up acidic gases from indoor air. In ResAM, we specify the initial conditions for the vapor pressure calculations as follows. The temperature is assumed to be slightly below body temperature (309.1 K) and the water activity of the particle is 0.952. This water activity is the average of water activity of an isotonic solution (Table S1) and the relative humidity at the exit of the nose or mouth (Table S4). Using ResAM, SLF is calculated to have a pH of 6.62 when in equilibrium with 23,550 ppm CO_2 and 133 ppb NH_3 in the gas phase (i.e., the average of the concentrations of these gases in the exhaled air plume and in typical indoor air; see section "Aerosol initial pH buffering"). For comparison, endoscopic nano-sensor studies of airway lining fluid find pH values *in vivo* of ~ 6.6 in the central airways of healthy humans (14, 15). We use this solution with water activity of 0.952 and pH 6.6 for the initial composition of all simulations in this work (except in Figs. S14A and S15A, which show the sensitivity to other initial pH values). In this reference, the molalities (in mol/kg-H_2O) of the involved species are: H_2O: 55.51, proteins with an effective molar mass 1000 Da: 0.094, lipids with an effective molar mass 190 Da: 0.322, Na^+: 1.371, Cl^-: 1.400, other cations: 0.1243, other anions: 0.097, $CO_2 + HCO_3^- + CO_3^{2-}$: 1.908×10^{-3}, $NH_3 + NH_4^+$: 1.257×10^{-3}. Other species are set to be zero.

Aerosol initial pH buffering

The pH of SLF is 6.6 in our reference case. However, the concentrations of buffer species such as bicarbonate and ammonia affect pH significantly and have to be treated properly. The acid-base pairs CO_2(aq)/HCO_3^- and NH_4^+/NH_3(aq) are major buffers in respiratory fluids(16, 17). The initial concentrations ($t = 0$) of CO_2, HCO_3^- and CO_3^{2-} are calculated assuming equilibrium with 23,550 ppm CO_2 in the gas phase (i.e., the mean of the concentrations of CO_2 in exhaled air and indoor air, see Table S4), which is an approximation for the internal mixing of inhaled and exhaled air in the respiratory tract. Similarly, we apply a mean concentration of ammonia. Depending on its composition and pH, the respiratory fluid takes up more or less CO_2 and, thus, contains more or less bicarbonate, which acts as an efficient pH buffer. This determines the initial properties of freshly formed expiratory aerosol particles, and also their readiness to subsequently take up acidic gases from the indoor air. The pH ~ 6.6 in the airways of healthy humans can be altered by disease or lung inflammation (15). To estimate the importance of deviations from the reference value of pH 6.6, we performed sensitivity runs with ResAM using an initial pH of 6.2 or 7.0. In the model, these pH values are achieved by adding small amounts of HCl or NaOH to the modeled SLF (while maintaining equilibrium with the mentioned CO_2 and NH_3 concentrations). In detail, pH 6.2 is achieved by adding 2.63×10^{-3} mol/kg-H_2O of HCl, and pH 7.0 by adding 2.66×10^{-3} mol/kg-H_2O of NaOH (for comparison, the Na^+ and Cl^- concentrations in the reference solution are larger than 1 mol/kg-H_2O). Consequently, the total concentration of dissolved CO_2 (i.e., CO_2(aq) + HCO_3^- +

CO_3^{2-}) varies between 1.1×10^{-3} mol/kg-H_2O at pH 6.2 to 3.8 $\times10^{-3}$ mol/kg-H_2O at pH 7.0. The transition from the release of an aerosol particle inside the respiratory tract to the exits (nose or mouth) is modeled by linear relaxation of the gas phase composition towards exhaled air given by Table S4 (i.e., CO_2 ramping up linearly from 23 550 ppm at the moment of particle formation to 46,500 ppm at the nostrils 70 ms later, before relaxing to 600 ppm by eddy mixing with the indoor air). The buffering effect is clear in Figs. S14A and S15A: in the model run with 50 ppb HNO_3, an initial pH of 7.0 leads to slower virus inactivation for particles with radii > 1 µm. However, initial pH plays only a minor role for smaller particles. Furthermore, initial pH makes hardly any difference for virus inactivation in typical indoor air (except for IAV in particles > 50 µm).

Ion-interaction modeling

The activity coefficients of H^+, Na^+, NH_4^+, Cl^-, NO_3^- and OH^- ions are calculated using the Pitzer ion-interaction model (18–20). For the anions CO_3^{2-}, HCO_3^- and CH_3COO^- with minor concentrations, we assume their activity coefficients in SLF to be unity (because of missing interaction parameters). The parameters for NaCl in the Pitzer-ion interaction model were recalculated based on both the data of Chan et al (21) and our own data on pure NaCl shown in Fig. S4. The water activity is calculated considering the contribution of the inorganic and organic species:

$$a_w \approx a_{w,\text{inorganic}} \times a_{w,\text{organic}}, \qquad \text{[S6]}$$

where the water activity of organic species and that of the ions with minor concentrations (CO_3^{2-}, HCO_3^-, CH_3COO^-) are calculated using Raoult's law:

$$a_{w,\text{organic}} = \frac{M_{H_2O}}{M_{H_2O} + \sum_j M_{\text{organics}^j}}, \qquad \text{[S7]}$$

where M_{H_2O} is the molality of water and M_{organics^j} is the molality of organic species (and j denotes the two organic categories, light and heavy).

Dissociation equilibria and pH

The aqueous phase dissociation constants are listed in Table S2. They are used independently in each model shell (following each diffusion time step). The H^+ concentration is obtained by setting the net charge in each shell to zero. The pH is then given by

$$\text{pH} = -\log_{10} a_{H^+}. \qquad \text{[S8]}$$

The vapor pressures of H_2O, NH_3, HNO_3, HCl and and CH_3COOH are then calculated using the Henry's law coefficients listed in Table S2 and the activity coefficients calculated from the Pitzer-ion interaction model.

The difference between partial pressures and vapor pressures of each species determines whether the gas phase is supersaturated or subsaturated with respect to the condensed phase, which in turn decides whether a given species is condensing or evaporating. These pressures (or the corresponding mole fractions) are shown in Fig. S11 for the simulation in Fig. 3. After ~ 100 s, the vapor pressure of HCl is higher than its partial pressure, leading to a steady replacement of Cl^- ions by NO_3^+ ions, and eventually to the full deliquescence of the salt crystal.

Further ResAM details II: diffusion processes in expiratory particles

Nernst-Planck Equation and electroneutrality

By means of our EDB measurements, we identified two distinct stages during crystal growth separated by an abrupt change (see Fig. 2). We interpret this as weak impedance by fast water diffusion in the first stage and strong impedance by slow ion diffusion in the second stage, i.e. $D_{\ell,\mathrm{H_2O}} \gg D_{\ell,\mathrm{ions}}$. The question why the ion diffusivities are so much smaller than the H_2O diffusivity is beyond the scope of this paper. In the literature that is little evidence for such drastically different diffusion coefficients. However, preliminary experiments in much simpler solutions (aqueous ammonium nitrate / sucrose solutions) reveal a similar behavior (not shown).

It is well-known that different ions in a liquid diffuse with different velocities. For example, from isotopic and NMR-measurements in aqueous salt solution, it is known that $D_{\ell,\mathrm{Na^+}} < D_{\ell,\mathrm{Cl^-}} \ll D_{\ell,\mathrm{H^+}}$(22), see Table S3. Given that H^+ ions are known to diffuse particularly fast, differences in Na^+ and Cl^- diffusivity could influence H^+ via electrostatic forces, which has immediate repercussions on particle pH. Therefore, it is critical to understand these microscopic transport processes.

When ions diffuse in a liquid, such as Na^+ and Cl^- in an expiratory particle, electroneutrality must be maintained (23), at least on scales much larger than the ions. Otherwise charge-separation would occur, resulting in physically unreasonably high electric fields. Therefore, either an ion of opposite charge diffuses in the same direction (salt diffusion) or an ion of the same charge diffuses in the opposite direction (counter diffusion). In these cases the flux will depend on the individual diffusion coefficients, the concentration gradients and the gradient of the electric potential, which arises from the tendency of one ion to diffuse faster than another. Electroneutrality is violated only on the nano-scale (nano with respect to space and time), as fluctuating hydrodynamics simulations reveal (24). As the H^+ ions participate in establishing charge neutrality, this affects the pH, albeit only marginally.

A proper treatment of ion diffusion requires to apply the Nernst-Planck Equation (25). The flux $\vec{j_i}$ of the species i at location $\vec{r}$ inside the particle is given by

$$\vec{j_i}(\vec{r}) = -D_{\ell,i}(\vec{r}) c_i(\vec{r}) \frac{1}{RT} \nabla \bar{\mu}_i, \qquad \text{[S9]}$$

where $D_{\ell,i}(\vec{r})$ is the liquid-phase diffusion coefficient of species i and $c_i(\vec{r})$ its concentration, T is the temperature of the liquid, and R the universal gas constant. The chemical potential of i in an electric field $\bar{\mu}_i$ is given by:

$$\bar{\mu}_i = \mu_i + z_i F \Phi(\vec{r}) = \mu_0 + RT \ln a_i(\vec{r}) + z_i F \Phi(\vec{r}), \qquad \text{[S10]}$$

where F is the Faraday constant, z_i is the electric charge of species i (= for neutral molecules, < 0 for anions, > 0 for cations), $a_i(\vec{r})$ its activity, and $\Phi(\vec{r})$ the electric potential. Inserting Eq. S10 into Eq. S9, we obtain the Nernst-Planck equation:

$$\vec{j_i}(\vec{r}) = -c_i(\vec{r}) \times \left(D_{\ell,i}(\vec{r}) \nabla \ln a_i(\vec{r}) + \frac{z_i F}{RT} \vec{E}(\vec{r}) \right), \qquad \text{[S11]}$$

where $\vec{E}(\vec{r})$ is the electric field. Together with the continuity equation, i.e. $\partial c_i / \partial t = -\nabla \cdot \vec{j_i}$, this becomes the diffusion equation for species i in an electric field:

$$\frac{\partial c_i}{\partial t}(\vec{r}) = -\nabla \cdot \vec{j_i}(r) = \nabla \cdot \left(D_{\ell,i}(\vec{r}) c_i(\vec{r}) \nabla \ln a_i(\vec{r}) + c_i(\vec{r}) \frac{z_i F}{RT} \vec{E}(\vec{r}) \right) \ . \quad \text{[S12]}$$

For neutral species, z_i equals zero, and the Nernst-Planck equation reduces to Fick's first law of diffusion. In Equation S11, $\vec{E}(\vec{r})$ is unknown, but can be obtained from the constraint of charge neutrality in the aerosol, i.e. by demanding zero net charge flux:

$$\sum_i z_i \times \vec{j_i} = \sum_i \left(-z_i \ \ c_i \ D_{\ell,i} \ \nabla \ln a_i - c_i \frac{z_i^2 F}{RT} \vec{E} \right) = 0 \quad , \quad \text{[S13]}$$

where the sum extends over all species i. Therefore:

$$\vec{E} = -\frac{\sum_i z_i \ \ c_i \ D_{\ell,i} \ \nabla \ln a_i}{\sum_i c_i \frac{z_i^2 F}{RT}} \quad \text{[S14]}$$

Inserting Eq. S14 into Eq. S11 enables us to determine the diffusion flux in the particle. ResAM divides the aerosol particle into shells (Fig. S2) and assumes the exhaled particle to have spherical symmetry, i.e,. net diffusion occurs only along the radial coordinate r. Hence, the rate of concentration change dc_i/dt in the shell with radius between r and $r + \Delta r$ equals:

$$\frac{dc_i}{dt} = \frac{4\pi r^2 j_i(r) - 4\pi (r+\Delta r)^2 j_i(r+\Delta r)}{V_i} = \frac{3r^2 j_i(r) - 3(r+\Delta r)^2 j_i(r+\Delta r)}{(r+\Delta r)^3 - r^3} \quad \text{[S15]}$$

This finalizes the treatment of diffusive fluxes of charged ions and neutral molecules in the interior of aerosol particle by the Nernst-Planck equation. These fluxes need to satisfy the boundary conditions at the interface to the gas phase and to the salt crystal in the case of efflorescence, discussed below.

Boundary condition at the liquid-gas interface

The flux $\vec{j_i}(r \to r_g)$ in the liquid at the particle interface with the gas phase, r_g ($= r_{n+1}$ in Fig. S2), is given by Eq. S16. This flux needs to consider the exchange of the volatile species with the gas phase, i.e. it needs to equal the flux at r_g in the gas phase. The exchange with the gas phase is calculated using the gas phase diffusion onto a spherical particle surface with radius r_g in steady state, given by(26):

$$j_{\text{surf},i} = 4\pi r_g D_{g,i} \frac{p_i^{\text{vap}}(T_{\text{ptcl}}) - p_i}{RT_{\text{air}}} \quad \text{[S16]}$$

with p_i being the partial pressure and p_i^{vap} the vapor pressure of species i, $D_{g,i}$ is the gas-phase diffusion coefficient of species i, T_{air} the indoor air temperature, and T_{ptcl} the temperature of the particle.

Boundary condition at the liquid-solid interface and dendritic crystal growth habit

SLF particles effloresce readily when RH drops below $\sim 56\%$ (Fig. 2). Before we treat the boundary condition for the Nernst-Planck equation, we pay attention to the complex dendritic growth habit of the NaCl crystal revealed by microscope images (Fig. S6). ResAM treats the crystal to be spherical and positioned in the particle center. However, the dendritic crystals resemble much more an ensemble of narrow cylinders with a surface area much larger than that of a compact sphere.

Thus, the diffusion of Na^+ and Cl^- ions to the dendritic surfaces is much faster than that to a sphere. The resulting differences can be approximately corrected by choosing an effective diffusion coefficient that compensates the surface ratio.

The number of Na^+ and Cl^- ions absorbing onto (or desorbing from) the dendritic cylinders per time unit (i.e. their diffusive flux integrated over the dendritic surface) is

$$\frac{dN_{Na^+/Cl^-}}{dt} \approx -2\pi\rho_c l_c \times c_{Na^+/Cl^-} \times D_{\ell,Na^+/Cl^-} \frac{\partial}{\partial\rho} \ln a_{Na^+/Cl^-}\Big|_{\rho\to\rho_c} \quad , \qquad [S17]$$

where ρ is the radial distance in cylindrical coordinates, ρ_c and l_c are the mean radius and total length of the dendritic cylinders. For comparison, the diffusive flux of the ions to a centered sphere is

$$\frac{dN_{Na^+/Cl^-}}{dt} = -4\pi r_s^2 \times c_{Na^+/Cl^-} \times D^*_{\ell,Na^+/Cl^-} \frac{\partial}{\partial r} \ln a_{Na^+/Cl^-}\Big|_{r\to r_s} \quad , \qquad [S18]$$

where r_s is the radius of the compact sphere with the same volume as the dendrites. We introduce effective diffusion coefficients of Na^+ and Cl^- ions (marked by a star), D^*_{ℓ,Na^+} and D^*_{ℓ,Cl^-}, which compensate the different shapes. Assuming the same activity difference between solid and liquid for both shapes, we obtain:

$$\rho_c \frac{\partial}{\partial\rho} \ln a_{Na^+/Cl^-}\Big|_{\rho\to\rho_c} \approx r_s \frac{\partial}{\partial r} \ln a_{Na^+/Cl^-}\Big|_{r\to r_s} . \qquad [S19]$$

Equating Eqs. S17 and S18 and considering Eq. S19 yields

$$D^*_\ell \approx D_\ell \frac{l_c}{2r_s} . \qquad [S20]$$

From the microscope images (Fig. S6), the total length of the dendrites in the droplet with radius of 20 µm is 340 µm. Assuming the thickness of the dendrites is independent of the aerosol particles size, the length of the dendrites is then proportional to the volume of the aerosol particle. The length of the dendrites with radius R_{ptcl} can be estimated as

$$l_c \approx \max\left(\frac{340}{20^3}\ \mu m^{-2}\ R^3_{ptcl}\ ,\ 2\times r_s\right) , \qquad [S21]$$

where the second term in the maximum expression $(2 \times r_s)$ becomes important for small particles and ensures that $D^*_\ell \geq D_\ell$. Typical enhancement factors D^*_ℓ/D_ℓ vary from 1 for $R_{ptcl} = 1$ µm to 4 for 10 µm to 400 for 100 µm.

We next derive the flux of ions across the solid/liquid interface, which constitutes the boundary condition for the Nernst-Planck equation. In this case, the electric force can be ignored, since the Na^+ ions and Cl^- ions must always diffuse to the crystal with the same rate, provoking no charge separation. Assuming the uniform activity coefficients in the shell adjacent to the solid crystal, an analytical solution for j_{Na^+/Cl^-} can be obtained:

$$j_{Na^+/Cl^-} = -4\pi D^*_{\ell,Na^+/Cl^-} \times r_s \frac{r_1 + r_s}{r_1 - r_s} \times \left(c_{Na^+/Cl^-}(r_1) - c_{Na^+/Cl^-}(r_s)\right) \quad . \qquad [S22]$$

Here, r_1 is the outer radius of the innermost liquid shell. The Na^+ and Cl^- concentrations at r_1 are determined from the Nernst-Planck equation of the liquid phase diffusion. At the crystal surface r_s, the solution is in equilibrium with the crystal, i.e. $a_{NaCl,solid} = a_{Na^+} a_{Cl^-}$. The activity product of solid NaCl, a_{NaCl}, is given in Table S2. Setting $j_{Na^+} = j_{Cl^-}$ and considering the solid equilibrium at the solid surface, the concentrations c_{Na^+}, c_{Cl^-} at r_s can be calculated, thus also the flux of Na^+ and Cl^- ions from/to the crystal.

Summary of diffusion coefficients in expiratory particles

The liquid phase diffusion coefficients at infinite dilution in water are summarized in Table S3. The liquid phase diffusion coefficients of Na^+ and Cl^- ions, D_{ℓ,Na^+} and D_{ℓ,Cl^-} at RH 50 - 70% are derived using the EDB data (Fig. S9). The very rapid mass loss immediately after nucleation of the NaCl crystal indicates rapid diffusion of H_2O (Fig. S9B,D number ④), while the further crystal growth due to diffusion of Na^+ and Cl^- ions is slow (Fig. S9B-D numbers ② and ③).

We assume that the liquid-phase diffusion coefficients of all neutral species (NH_3, CO_2, CH_3COOH, NH_4CH_3COO, etc.) have the values provided in Table S3 for infinitely diluted solutions and follow the same water activity dependence as H_2O molecules in more concentrated solutions ($D_{\ell,H_2O}(a_w)$). Similarly, the diffusion coefficients of all ions (NH_4^+, NO_3^-, CH_3COO^-, HCO_3^-, etc.) have the values provided in Table S3 for infinitely diluted solutions and follow the same water activity dependence of Na^+ and Cl^- ions in more concentrated solutions, as shown in Fig. S9.

In addition, we assumed that all diffusion coefficients have the same temperature dependence as that of citric acid (27). The error introduced by this approximation is small, because the temperature range relevant for exhalation under indoor conditions is narrow (293.15 K to 307.15 K). The particle temperature of the exhaled particles is calculated considering the latent heat of the evaporating water.

In summary, the use of the Nernst-Planck equation ensures a physically consistent treatment of ion diffusion inside the expiratory particles. The H^+ ions participate in establishing charge neutrality, which affects the pH. In ResAM we treat the diffusion problem using the Nernst-Planck equation with $D_{\ell,Cl^-} \approx 1.5 \times D_{\ell,Na^+}$ and adjust all anion and cation diffusivities according to Table S3. We compared these runs with runs assuming $D_{\ell,Na^+} = D_{\ell,Cl^-}$ (with concentrations gradients instead activity gradients) and find pH differences of up to 1 pH unit during times of highest pH gradients (around 1 s in the expiratory plume). This demonstrates the importance of different anion-cation diffusivities and their treatment in the Nernst-Planck formulation, which cannot be ignored in the present application.

Further ResAM details III: simulation of virus inactivation and transmission risks

Mixing of the exhaled aerosol with indoor air

In our analysis, we do not consider spatial heterogeneities in the gas-phase concentration of water vapor and gas-phase precursors, but rather a mean field of these parameters and their gas-to-particle transfer controlled by diffusion; this is equivalent to focusing on the virus-containing aerosol outside of the "puff phase" (order of a few seconds), where acidification of the particles would have not occurred to a substantial degree (28–30). The particles considered are persistent and can remain airborne for many minutes to hours, given that the relevant particles have diameters of 5 µm and less (28), hence small settling velocities and gas-to-particle mass transfer in the vicinity of particles

controlled by molecular diffusion (Stokes Regime). The gas phase compositions of exhaled air, typical indoor air and various indoor scenarios are provided in Table S4. In our model simulations we use 20°C (293.15 K) as typical indoor temperature and 34°C (307.15 K) as initial temperature of exhaled air (31). We simplified the exhaled air plume as a two-dimensional air flow. The dispersion of the exhaled plume is then approximated using the mean square diffusion length in a 2-D system(32):

$$< r^2 > = 4\ D_{g,\text{eddy}}\, t. \qquad \text{[S23]}$$

$D_{g,\text{eddy}}$ is the turbulent eddy diffusion coefficient of the air inside the room under consideration, which we calculated following Shao and coworkers. They showed that $D_{g,\text{eddy}}$ is a function of the air exchange per hour (ACH) used during indoor mixing ventilation, i.e. $D_{g,\text{eddy}} = f(\text{ACH})$(33). The cross section of the exhaled air plume with an initial area $A(0)$ is then given by

$$A(t) = A(0) + \pi < r^2 >= A(0) + 4\pi D_{g,\text{eddy}} t, \qquad \text{[S24]}$$

and the corresponding gas phase mole fraction or mixing ratio ($\chi(t)$) in the diluting exhaled plume including H_2O is

$$\chi(t) = \frac{A(0)}{A(t)}\chi_{\text{exhaled air}} + \frac{A(t) - A(0)}{A(t)}\chi_{\text{indoor air}}. \qquad \text{[S25]}$$

The relative humidity is then the ratio of partial pressure (i.e., the total pressures × H_2O mole fraction) over the vapor pressure of pure water(34). For normal breathing, we assume an initial area $A(0) = 2 \times \pi \times 0.75^2$ cm^2 (corresponding to the size of two nostrils with radius of 0.75 cm). Shao et al. (33) report $D_{g,\text{eddy}}$ values for an ACH range from 0.43 to 2.97 based on their experiments using toluene and acetone. The temperature of the exhaled air plume is calculated analogously to the gas phase mixing ratio (see Eq. S25).

For ACH = 2, we use $D_{g,\text{eddy}} = 50$ cm^2/s in the present simulations. For ACH = 0.1, we use the lower limit $D_{g,\text{eddy}} = 10$ cm^2/s (33). We note that $D_{g,\text{eddy}}$ is roughly proportional to ACH^2 (see Table 3 of Shao et al.(33)). Thus, we extrapolate $D_{g,\text{eddy}}$, and obtain $D_{g,\text{eddy}} = 1250$ cm^2/s for ACH = 10.

The exhaled aerosol exchanges semi-volatile species with the gas phase. Nazaroff and Weschler reviewed the indoor air acids and bases (35). The gas phase composition is given by Table S4. By adding HNO_3 to the indoor air, the partitioning of NH_3 will change: the lower pH of background indoor aerosol allows more uptake of NH_3, i.e. NH_3 is scavenged by the background aerosol (see again Table S4). The reduction of NH_3 by adding HNO_3 to the indoor air is calculated assuming an aerosol mass concentration of 20 µg/m^3, which is a typical value for household indoor air (36). We use a simplified composition of background aerosol of aqueous sucrose/sulfate/Cl^-/NO_3^- solution. Our final results are not strongly dependent on aerosol mass concentration or composition. Under typical indoor conditions, 20°C and 50% RH, the gas phase NH_3 is reduced from 36.3 ppb to 1.88 and 0.376 ppb, by enriching indoor air to 10 ppb and 50 ppb HNO_3, respectively.

The composition and pH of the exhaled aerosol is calculated for sizes ranging from 0.2 µm to 1000 µm. In combination with the measured inactivation time of virus at given pH, the 99%-inactivation time of viruses in the exhaled aerosol can then be readily calculated. The resulting composition, pH and virus concentration in exhaled aerosol are shown in Fig. 4 for 50% RH and by Fig. S10 by for 80% RH.

Virus inactivation times and residual infectious fractions in aerosol particles

In the aerosol phase, the extent of virus inactivation in a microscopic particle depends on particle size, pH-dependent inactivation processes, and the time since exhalation. As prerequisite for the treatment of the microscopic aerosol problem, we use our macroscopic inactivation measurements shown in Fig. 1 (based on matrix volumes between 10 µl and 1 ml), to derive 1/e-inactivation times, τ, for all three viruses. These bulk measurements provide τ as a function of pH and of the mass fraction of solutes, x_m, which we fit for convenience to arctan functions. For IAV, we approximate the inactivation times by the following fit:

$$\begin{aligned}\tau(\mathrm{pH}, x_m)/\mathrm{s} = &\exp(-2.045 + 0.46916 \times \mathrm{pH}) + \\ &\exp\Big[5.0131 + 6.2214 \times \arctan\Big(1.2972 \times \\ &(\mathrm{pH} - 5.41836 + 1.4134 \times x_m) \times (1.012728 - 0.4714 \times x_m)\Big)\Big]. \end{aligned} \quad \text{[S26]}$$

Based on Eq. S26, Fig. 1 shows the calculated 99%-inactivation times for different solute mass fractions (blue curves).

The inactivation time of SARS-CoV-2, which shows no strong dependence on x_m over the measured range (see Fig. 1), is expressed as a function of pH by

$$\tau(\mathrm{pH})/\mathrm{s} = \exp\Big[4.25622 + 5 \arctan\Big(2.0308 \times (\mathrm{pH} - 2.1729)\Big)\Big]. \quad \text{[S27]}$$

Finally, the inactivation time of HCoV-229E as a function of pH is expressed by

$$\tau(\mathrm{pH})/\mathrm{s} = \exp\Big[8.3045 + 3.3891 \arctan\Big(0.50961 \times (\mathrm{pH} - 2.2457)\Big)\Big]. \quad \text{[S28]}$$

Next, we determine $N(R_0, t)/N(R_0, 0)$, which is the residual infectious virus fraction at time t in an aerosol particle exhaled at time $t = 0$ with initial radius R_0 . In shell k, the infectious virus fraction is given by

$$\ln \frac{N_k(R_0, t)}{N_k(R_0, 0)} = -\int_0^t \frac{dt'}{\tau(\mathrm{pH}_k(t'), x_{m,k}(t'))} \,. \quad \text{[S29]}$$

Here, $N_k(R_0, 0)$ and $N_k(R_0, t)$ are the number of infectious viruses in shell k at time 0 and time t, respectively, and $\mathrm{pH}_k(t')$ and $x_{m,k}(t')$ are the simulated pH and mass fraction of solutes of shell k at time t'. For the entire particles, the infectious fraction of virus, $N(R_0, t)/N(R_0, 0)$, is given by

$$\frac{N(R_0, t)}{N(R_0, 0)} = \frac{\sum_k N_k(R_0, t)}{\sum_k N_k(R_0, 0)}. \quad \text{[S30]}$$

Note that the summation over shells in Eq. S30 results in a volume-weighted averaging for the inactivation times. The times for e-folding, 10^{-2}- and 10^{-4}-fold reductions calculated from Eq. S30 as a function of initial particle radius R_0 are shown in Fig. 4.

Modeling of indoor airborne viral load and relative risks of transmission

To estimate the risk of transmission we assume that it is linearly proportional to the calculated airborne viral load. The "relative transmission risk" then refers to the change in risk from standard conditions (here typical indoor air according to Table S4) compared to treated air. The airborne load of infectious viruses depends on the emission rate of these viruses on the one hand (source), and the deposition of aerosol particles, the ventilation of indoor air, and finally the inactivation of viruses in aerosol particles on the other hand (sinks). Assuming well-mixed ventilation, the airborne viral load (number of infectious viruses per volume of air) can be expressed as

$$\bar{n}_{\mathrm{virus}}(t) = \frac{1}{V}\int_0^t \int_{50\,\mathrm{nm}}^{\infty} \nu(R_0)\,\frac{dQ}{d\log(R_0)}\,f_{\mathrm{depo}}(t-t')\,e^{-\mathrm{ACH}\times(t-t')}\,\frac{N(R_0,t-t')}{N(R_0,0)}\,d\log(R_0)dt'. \quad [S31]$$

Here , V is the room volume occupied per infected person, $dQ/d\log(R_0)$ is the aerosol number emission rate distribution of one human (see Fig. 4E), $\nu(R_0)$ is the number of virus in one aerosol particle of radius R_0 and $N(R_0,t-t')/N(R_0,0)$ is the residual infectious virus fraction (see Eq. S30). (In passing we note that $dQ/d\log(R)$ in Fig. 4E refers to $t = 1$ s, which we take into account by extrapolating backward to $t = 0$ in Eq. S31.) Finally, $f_{\mathrm{depo}}(t-t')$ is the reduction factor due to deposition, given by

$$f_{\mathrm{depo}}(t-t') = e^{-\int_0^{t-t'} \frac{v_{\mathrm{dep}}(R(t''))}{h}dt''}, \quad [S32]$$

where $v_{\mathrm{dep}}(R)$ is the deposition velocity of aerosol particles with radus R, and h is the height of the room.

We assume V is 10 m^3 per infected individual, and the height of room h is 2 meters, which represents a typical length scale for deposition (assuming the indoor air to be well-mixed due to convection and turbulence and irrespective of the particular position of the infected human). The emission rates of exhaled aerosol during breathing, coughing and speaking/singing shown in Fig. 4E from Pöhlker et al. (37) are used. We calculate the particle deposition velocity v_{dep} from experimentally determined dry deposition data (Seinfeld and Pandis, 2006; Fig. 19.2, data for $u^* = 44$ cm/s(38)). A slower deposition velocity ($u^* = 11$ cm/s) results in an even stronger decrease in the relative risks of transmission. The steady state airborne viral load can be calculated by integrating Eq. S31 over a sufficiently long time t, such that the viral load converges to a constant value, $\bar{n}_{\mathrm{virus}}(t \to \infty)$.

Results for $\nu(r) \equiv 1$, i.e. each aerosol particle containing one virus, are shown in Figs. 5 and S19. Results for $\nu(r) \propto r$, i.e. virus concentration that are proportional to the size of the aerosol particles, are shown in Fig. S18. Also for $\nu(r) \propto r$, significant reductions of transmission risks can be achieved by air acidification for all kinds of emissions (breath, cough, speak/sing).

Indoor air gas concentration for different ACHs

The ventilation (ACH) affects the indoor gas phase concentration. Gases with mainly outdoor sources (e.g. HNO_3 and HCl) have higher concentrations at higher ACH. Conversely, gases with mainly indoor sources (e.g. NH_3, CO_2, acetic acid) have lower concentrations at higher ACH. We estimated the gas phase concentration for 10 ACH and 0.1 ACH as follows: gas phase concentrations and their upper and lower limits are given in Table S4 for 2 ACH. For HNO_3 and HCl, assuming no indoor source and a deposition velocity of 0.5 cm s^{-1} (see Figure 19.2 of (38)), the estimated outdoor

concentrations from the values in Table S4 are comparable with the values given by (35). From this, the indoor concentration of HNO_3 and HCl at 10 ACH and 0.1 ACH can be calculated. For NH_3 and acetic acid, it is assumed that the outdoor concentration is reduced by an factor of 10 and 15 compared to indoor air, respectively (35). The outdoor CO_2 concentration is set to be 415 ppm. The indoor emission rate can be estimated for NH_3, acetic acid and CO_2 for a deposition velocity of 0.05 cm s^{-1} (assuming an uptake coefficient of 0.1) and the indoor gas phase concentration for ACH. Again, the indoor gas phase concentration for 10 ACH and 2 ACH can be calculated.

ResAM sensitivity studies

We performed sensitivity analyses for the modeled inactivation times of IAV and SARS-CoV-2 by systematically varying eight critical model parameters (Figs. S14 and S15. The following listing by capital letters refers to the sensitivity model runs depicted in the various panels of these figures:

A: Sensitivity to initial pH buffer strength of exhaled aerosol. In the model runs presented in this paper, the initial pH during particle formation is 6.6. Sensitivity tests were performed with ResAM for initial pH of 6.2 or 7.0 (see subsection "Aerosol initial pH buffering" for details). An initial pH of 7.0 leads to slower, and an initial pH of 6.2 to faster virus inactivation for particles with radii > 1 µm, in particular in acidified air. The effect of initial pH is less important for smaller particles, which are dominant during exhalation. Note that the sensitivity test for pH 7.0 covers also the case with original SLF concentrations initially in equilibrium with 46,500 ppm CO_2.

B: Sensitivity to mixing speed of exhaled air plume with indoor air. A longer mixing time, i.e. a smaller eddy diffusion coefficient $D_{g,\mathrm{eddy}}$ (see Eq. S23), has only a weak effect, leading to slightly longer inactivation times.

C: Sensitivity to uncertainties in liquid phase diffusion coefficients. The exact value of the liquid phase diffusion coefficient plays a critical role for aerosol particles with radius larger than about 1 µm. The impact becomes negligible for small particles, when inactivation times are short anyway and are governed by the mixing with the indoor air (via $D_{g,\mathrm{eddy}}$) or by the virus inactivation time.

D: Sensitivity to NH_3 gas phase mixing ratio. In typical indoor air, an increase in the gas phase NH_3 mixing ratio increases the inactivation time negligibly. Conversely, a nearly complete removal of NH_3 decreases the inactivation time only for exhaled particles with radii > 1 µm, but also this becomes negligible when the air is enriched with HNO_3.

E: Sensitivity to HNO_3 gas phase mixing ratio. In typical indoor air, the inactivation time of IAV changes only slightly, when the HNO_3 gas phase concentration varies by a factor of 2, and only for exhaled aerosol particles with radius > 1 µm. However, the pH of the exhaled aerosol remains above 6, when there is no HNO_3 and HCl in the gas phase and the inactivation time becomes $> 10^5$ s, independent of their size.

F: Sensitivity to indoor temperature. Inactivation times slightly decrease with increasing temperature. Neither the temperature dependence of the different physicochemical model parameters, nor that of virus inactivation kinetics, critically affect the inactivation times.

G: Sensitivity to relative humidity. The higher the relative humidity, the shorter the inactivation time. However, the differences remain small in the RH range 40 - 80%.

H: Sensitivity to aerosol matrix composition. Depending on the inorganic/organic ratio, the activity coefficients may differ, which in turn affects virus inactivation times. Assuming unchanged liquid phase diffusion coefficients, we performed sensitivity runs reducing the composition to only the organic components of SLF or to pure NaCl. The computed inactivation times typically differ by less than 50% from those of SLF.

Supporting Text

Uncertainties and validity limitations

The combination of virus inactivation data from bulk phase measurements (Fig. 1) with the aerosol microphysical thermodynamics (vapor pressures and activity coefficients) and kinetics (Figs. 2 and S9) allows us to determine the pH in aerosol particles and the resulting rates of viral inactivation. To this end we use the biophysical model of inactivation in expiratory aerosol particles ResAM (Figs. 3-5 and SI). Each of these three elements as well as their combination involve a number of limitations and assumptions that must be considered to avoid misapplications of this work. Safe applications are limited to the factual data and parameter ranges listed below.

Limitation to investigated viral strains. Our results refer to influenza virus strain A/WSN/33 (H1N1), SARS-CoV-2 strain BetaCoV/Germany/BavPat1/2020 and the coronavirus strain HCoV-229E-Ren. The comparison of our results for SARS-CoV-2 and HCoV-229E-Ren demonstrates how different the pH-sensitivity of coronaviruses can be. Hence, the applicability of our results to other strains is not given and needs to be addressed in future work.

Representativeness of the investigated matrices. In both experimental parts of the present work, virus inactivation in bulk measurements and microphysical investigations in the EDB, we studied SLF and nasal mucus. The results for these two matrices are remarkably similar, suggesting that SLF is a good synthetic substitute for mucus, with an appropriate mixture of proteins, lipids and salts. However, other body fluids, such as bronchial mucus or saliva, might behave differently and need to be investigated in future work.

Validity range of indoor temperature 15°C $< T <$ 25°C. Our virus inactivation measurements refer to 20°C and our EDB measurements to 15°C. When the temperature is increased by 5°C, we (conservatively) estimate virus inactivation rates to increase by 50% (based on results in (39)), and by 3% due to faster liquid phase diffusion (assuming the same temperature dependence as that of H_2O in citric acid (27)). The temperature dependence of other factors, such as Henry's law coefficients (vapor pressures) and dissociation coefficients are included in the model, with very small uncertainties, or are known only at room temperature, as for some interactions parameters (Na^+, NO_3^-, Cl^-). However, neither the temperature dependence of the physicochemical parameters, nor that of virus inactivation kinetics, critically affect the inactivation times. The overall error caused by these approximations is likely to be small (less then a factor of 2 in inactivation times), because the temperature range relevant to exhalation under indoor conditions is narrow (15°C-34°C).

Validity range of indoor relative humidity $RH \leq$ 50%. Our virus inactivation measurements refer to water activities a_w = 0.994, 0.97 and 0.80 (i.e., RH = 99.4%, 97% and 80%, when the matrix – SLF or nasal mucus – is in equilibrium with water vapor in the gas phase), corresponding to the original SLF recipe (1×SLF), and to concentrated solutions 5×SLF and 18×SLF, respectively. Experiments at a water activity of 0.5 (24×SLF) are experimentally inaccessible (due to efflorescence), but need to be extrapolated. The protection is caused by substances in the SLF (e.g., proteins, salts). We have assumed their effect to be proportional to their concentration (dotted curve in Fig. 1). If it was proportional to a_w, their effect could lead to 99%-inactivation times longer by factors 2-20. However, Lin et al. (40) suggest that the protective effect of proteins in the case of bacteriophages is concentration-proportional at high RH (80%), but is not as effective at lower RH (20-50%). Therefore, we assume that the concentration-proportional extrapolation is reasonable and might even be an overestimation of the protective effect of SLF at low RH.

Uncertainties in results for typical indoor air (NH_3 = 36.3 ppb, HNO_3 = 0.27 ppb, HCl = 0.237 ppb, CH_3COOH = 48.7 ppb, and CO_2 = 600 ppm). The "typical" indoor air values used here (Table S4) refer to the weighted averages of all indoor values with natural ventilation or window air conditioners, excluding air in libraries and museums (Nazaroff and Weschler (35)). Uncertainty ranges (min-to-max) are large, sometimes including values below instrument thresholds. However, even under extreme conditions, buffering may lead to insensitive pH response. E.g., Fig. S14E shows that inactivation proceeds even without any indoor HNO_3, as the loss of HCl from the particles is partly compensated by the presence of gas phase HCl. Only if both, HNO_3 and HCl are absent, 99%-inactivation times stay above 10^4 s. Figures S14 and S15 show the sensitivities of virus inactivation to each individual parameter, not to their combinations. Hence, the term "typical indoor air" refers only to the values stated in Table S4.

Uncertainties in initial conditions of exhalation aerosol. There is large variability in exhalation air, e.g. in NH_3 differing a lot depending on whether exhalation occurs through the mouth or the nose. Furthermore, the concentration of initial HCO_3^-, an important buffer, depends on the current state of mixing of younger, inhaled air with low CO_2 and old air with high CO_2 content in the bronchiole. Both, dissolved NH_3/NH_4^+, and HCO_3^-, determine the initial pH of exhalation particles. Using ResAM, SLF is calculated to have a pH = 6.62, when in equilibrium with 133 ppb NH_3 and 23,550 ppm CO_2 (i.e., the mix between 46 500 ppm for air that has been completely consumed by breathing and 600 ppm for indoor air). Figures S14A and S15A show the sensitivities of shifting the initial pH by ± 0.4 pH units. Note that the sensitivity test for pH = 7.0 covers the case with SLF concentrations initially in equilibrium with 46,500 ppm CO_2. (We also note that breath condensates sampled in medical treatments typically have an alkaline pH, but only after degassing (41) and, hence, are not relevant in the present context.) The sensitivity tests show that the initial pH affects mainly the larger expiratory aerosols (emitted while speaking or coughing) and mainly under conditions with enhanced indoor acidity.

Approximation as droplet with concentric salt core, leaving the virus exposed to the liquid. The concentric shell model ResAM with volume-weighted probability for the location of the virus in one of the shells reduces the treatment to a one-dimensional problem (radial distance coordinate only). ResAM provides an accurate description of the inactivation process in a fully liquid particle, e.g. at RH = 80%. When efflorescence occurs (i.e., at $RH \leq 56\%$), dendritic crystal growth destroys the spherical geometry. A full three-dimensional treatment is beyond the scope of this paper. We approximate the three-dimensional nature of salt crystal growth by "effective" diffusion coefficients, which represent the molecular diffusivities under the specific morphological conditions of dendritic growth. While this is a reasonable approximation of the physicochemical processes, it assumes that the virus remains in the fluid. We have no information about whether the virus might be encased by the growing salt crystal, which could lead to a protection of the virus or to its mechanical destruction, i.e. to a delay or acceleration of the inactivation process. A delay of inactivation is likely to remain moderate, as impurities (as H^+ and NO_3^-) diffuse along veins in the triple junctions of crystals, producing a high conductivity solution-vein network (42) and connecting the virus with the liquid environment and its pH levels. This needs to be addressed in future work.

Uncertainties in our approach to risk modeling. Our estimate of the airborne viral load under steady state conditions in a single room with one infected person per 10 m^3 only allows to provide estimates of the relative risk of transmission. The infected person generating aerosol is assumed to provide a constant generating source, whereas is it not clear if IAV and SARS-CoV-2 are aerosolized at a constant rate. Also, if the volume per person is much smaller (e.g., only 5 m^3), total

risk increases, but the relative risk reduction by acidification grows (as NH_3 scavenging becomes more important). The model approach assumes perfect mixing of the air within the space, replacing a complex puff modeling by a simplified eddy diffusion modeling. Inactivation times can be longer in rooms with imperfect mixing or air stagnation. However, as we are only interested in providing coarse estimates of the relative risk of transmission, many of these complications affect the various air treatments (enhanced ventilation, removal of NH_3, addition of acidic gases) alike, allowing the relative changes to be estimated with reasonable confidence.

Comparison of published inactivation data with ResAM simulation

Figures S16 and S17 present a comparison of the 99%-inactivation times computed by ResAM (highlighted in green) with published measurements (colored circles). Previous work on IAV and SARS-CoV-2 in aerosol particles has focused on the dependence on RH, but did not consider the role of other air constituents that may modulate aerosol pH. The published data for IAV suggest a weak decrease of 99%-inactivation times with RH (Fig. S16). This trend is also captured by ResAM, and can be attributed to the increasing liquid phase diffusivity at higher RH. ResAM computation furthermore reveals a strong dependence of IAV inactivation time on air composition, and to a lesser extent on particle radius. Air filtration, e.g., by HEPA filters, can be expected to partly remove both organic and inorganic acids and bases, leading to a net increase in aerosol pH, and hence to prolonged inactivation times. In contrast, air conditioning by HNO_3 leads to aerosol acidification and shorter inactivation times. Published inactivation data for aerosolized IAV are consistent with ResAM estimates, assuming that experiments were conducted in partially purified air. Air treatment prior to experimentation in rotating drums was described in two studies (43, 44), and includes HEPA filtration and hydrocarbon traps. While earlier studies did not specify if air treatment took place, we can assume that all rotating drum experiments use filtered air to minimize contamination by ambient aerosol particles. According to ResAM model predictions, these treatments typically resulted in air purification of 80-99%.

SARS-CoV-2 exhibits little dependence on RH, as seen in both published data and in ResAM computations (Fig. S17). For this virus, ResAM determines only small variations in inactivation times due to air purification, because SARS-CoV-2 is insensitive to the ensuing changes in aerosol pH (Fig. 4). When air is amended with HNO_3, however, the resulting increase in aerosol acidity causes inactivation times shift to lower values. A comparison of inactivation times between published data and ResAM estimates is inconclusive. Due to the high stability of SARS-CoV-2 in unconditioned air, inactivation kinetics are difficult to measure in short-term rotating drum experiments. Consequently, inactivation rate constants exhibit large variability and inactivation times span over a wide range, even when determined under identical experimental conditions. Nevertheless, we observe that published inactivation times coincide with ResAM model results for typical room air all the way to fully purified air.

We conclude that ResAM is capable of reproducing inactivation trends of IAV and SARS-CoV-2 as a function of RH, as well as inactivation times under reasonable assumptions of the experimental conditions used. We furthermore note that in particular for pH-sensitive viruses, knowledge of air composition is critical to interpret and reproduce experimental results.

Investigation of CH_3COOH as potential agent against airborne viruses

Acetic acid enrichment does not enhance virus inactivation times

Based on an ancient medical custom (45), the boiling of vinegar as preventive measure against airborne pathogens has a long tradition, even though it remains unclear whether there is a scientific basis or whether it is folk tale. In February 2003, during the early phase of the Severe acute respiratory syndrome (SARS) outbreak in China, local media listed some preventive measures, including enhanced ventilation or using vinegar fumes to "disinfect the air", leading to vinegar being sold out in some cities (46). Diluted household vinegar containing 0.4-0.8 wt% acetic acid (CH_3COOH) was shown to reduce the infectivity of Human Influenza A/H1N1 in tissue culture by 7 orders of magnitude in less than 1 minute (47), and even against SARS-CoV-2 there is evidence of (CH_3COOH) being antiviral (48). However, the results of these in vitro experiments, which use well-mixed bulk volumes with a prescribed pH, are not directly applicable to aerosol particles freely floating in a gas. Whether a substance, such as CH_3COOH, readily partitions from the gas to the particulate phase depends on its volatility and on whether it may lead to sufficiently fast virus inactivation inside the particles. This, in turn, depends on a variety of aerosol properties and processes, which determine the disinfecting power of the substance, e.g., by attaining a high acidity or oxidation potential. Indeed, our measurements of CH_3COOH vapor pressure (see below) and model simulations (see Fig. S12) demonstrate that CH_3COOH is too volatile and a too weak acid to enhance virus inactivation, at least at concentrations below the permissible exposure level of 10 ppm.

Measurements of vapor pressure of ammonium acetate

To estimate the partitioning of gas phase acetic acid and ammonia in equilibrium with condensed phase ammonium acetate we measured evaporation rates of single, aqueous ammonium acetate particles levitated in the EDB. Details of the technique and data analysis were previously described (e.g. (49, 50)). Briefly, an aqueous ammonium acetate particle (ca. 15 µm radius) was injected into the EDB at a temperature of 20.4°C and 87.5% RH, and its mass evaporation rate was measured by the voltage compensating the particle's gravitational force. Analyzing nineteen such experiments yielded a vapor pressure of 0.12±0.05 Pa for ammonia and of 0.062±0.010 Pa for acetic acid.

Supporting Figures

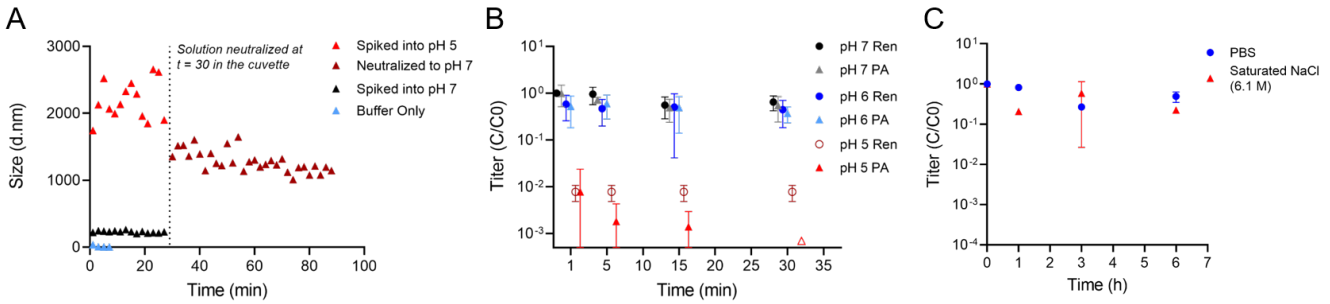

Fig. S1. Effect of virus aggregation on the infectivity of IAV. (**A**) IAV particle diameters were measured by DLS in PBS adjusted to pH 7 or pH 5. After 30 min the latter was neutralized to pH 7. The average diameter was measured every 2 min over a total time of 90 min. At pH 7, the average particle size was stable and corresponds to the diameter of monodisperse IAV particles (between 100 - 200 nm). The average particle diameter immediately increased to 1800 nm at pH 5, indicating rapid aggregation. The mean diameter then fluctuated between 1900 – 2600 nm for the full 30 minute period, indicating these aggregates were not transient. Upon neutralization to pH 7, aggregation was only partly reversed and the mean particle diameter remained above 1000 nm for the remainder of the time-course. (**B**) Infectivity of WSN/33-Renilla IAV particles over time in PBS adjusted to either pH 7, pH 6 or pH 5. WSN/33-Renilla harboring a gene encoding Renilla luciferase instead of the HA gene was generated as previously described (3). The titer was determined by both plaque assay and Renilla luciferase assay. While the titer measured by plaque assay (PA) indicates the number of infectious units, the titer measured by Renilla assay (Ren) correlates with gene expression. Both plaque and Renilla assay indicate the same decrease in infectivity as a function of pH, confirming that virus titer loss is associated with inactivation (i.e., loss in viral gene expression), not solely aggregation. Values below the LoD are indicated with empty symbols. Residual titer fractions were derived by normalization of measured titers (C) to the initial titer (C_0). (**C**) Infectivity of A/WSN/33 IAV particles over time in PBS and saturated NaCl solution. No effect of high ionic strength on infectivity was observed over the timescale of the experiment (6h), indicating that osmotic pressure does not impact influenza virus infectivity.

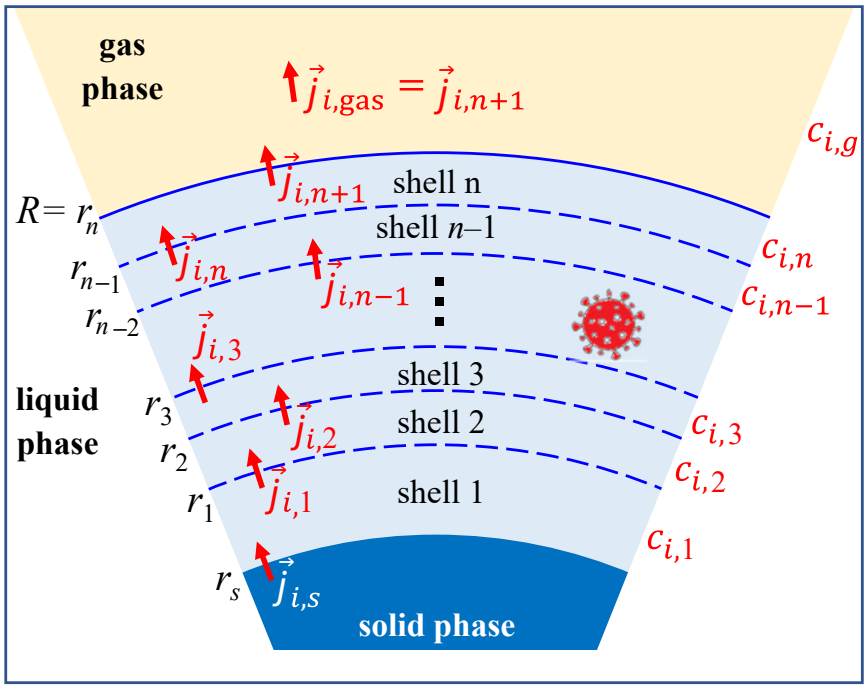

Fig. S2. Illustration of the discretization scheme used in the biophysical diffusion model ResAM. A spherical particle of radius R is divided into n concentric liquid shells plus a solid salt core of radius r_s (if efflorescence occurred). In each time step, changes in the concentration $C_{i,k}(t)$ of species i in shell k are calculated by fulfilling the liquid phase diffusion equation (Eq. S12), i.e. from the continuity equation balancing the diffusion fluxes $\vec{j}_{i,k}(t)$ into and out of the shell with concentration changes in the shell. The flux in the gas phase fulfills the gas phase diffusion equation. The flux into or out of the particle is calculated by equating $\vec{j}_{i,n+1}(t)$ with the flux in the gas phase of species i above the particle surface. The flux from or to the solid core, $\vec{j}_{i,s}(t)$, is calculated using Eq. S22.

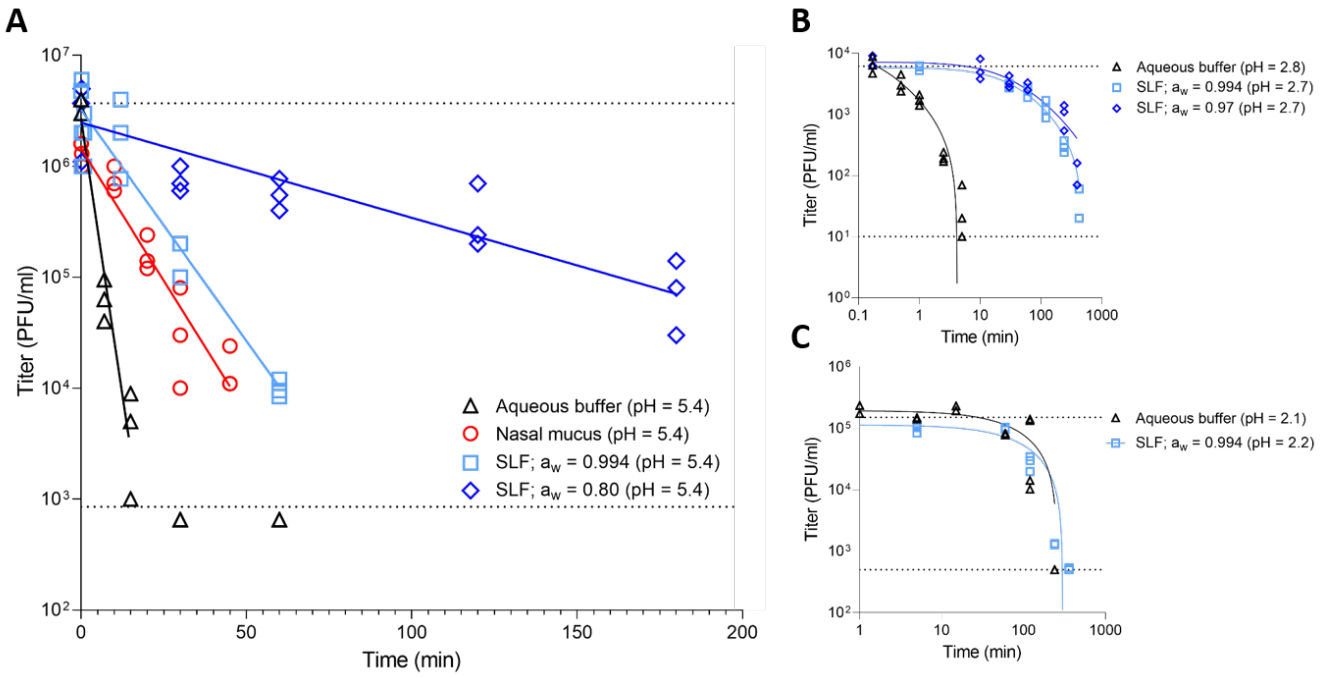

Fig. S3. Examplary inactivation curves of IAV, HCoV-229E and SARS-CoV-2 measured in aqueous buffer, in nasal mucus, and in different synthetic lung fluid (SLF) concentrations. (**A**) IAV, (**B**) SARS-CoV-2, and (**C**) HCoV-229E titers as a function of exposure time at a pH of 5.4, 2.7 - 2.8, or 2.1 - 2.2, respectively. Individual data points indicate triplicate measurements at each time-point. Solid lines represent model fits assuming first-order decay. Dashed lines correspond to the average starting titer (top line) and detection limit (bottom line) for each respective virus.

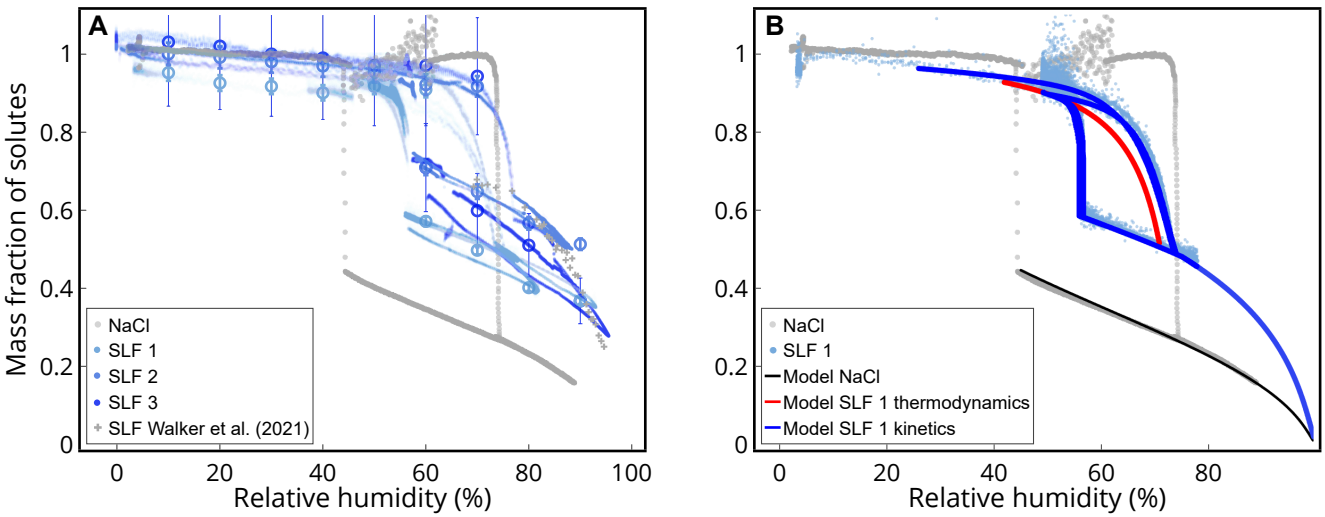

Fig. S4. Thermodynamic equilibrium properties of synthetic lung fluid (SLF). (**A**) Voltage data obtained from EDB measurements, converted to mass fraction of solutes (MFS), shown for one NaCl particle (NaCl - grey dots) and three different SLF particles (SLF 1 - light blue dots, shown also in Fig. 2, SLF 2 - medium blue dots, and SLF 3 - dark blue dots) during deliquescence/efflorescence cycles. Light grey crosses indicate measurements of SLF particles by Walker et al. (51). Open circles indicate the average for wet and dry conditions with error bars indicating the systematic error of the measurement (± 0.5 V). The hygroscopicity of the SLF particles are significantly smaller than of aqueous NaCl particles, but show large variability between different particles (beyond measurement uncertainty) owing to the large degree of multi-scale granularity of natural or synthetic lung fluids (see TEM images in Fig. S7). Note that MFS above 1 are an artifact due to very small changes in voltage under very dry conditions resulting in very large changes in MFS. (**B**) The thermodynamic equilibrium properties of the biophysical model ResAM were constrained using the data in **A**. Grey dots indicate NaCl as in **A**. Light blue dots indicate SLF 1 (as in **A** but only cycles 2 and 3). Curves show model results of ResAM. The black curve indicates modeled pure NaCl solution. The lower branch of the red solid curve indicates thermodynamic equilibrium behavior of SLF as function of RH, calculated by adjusting the activity of the organic fraction of SLF, $a_{\mathrm{org}} = f(a_w) = f(\mathrm{RH})$ to fit the EDB measurements. The upper branch of the red solid curve is the deliquescence curve of SLF in thermodynamic equilibrium as calculated by ResAM, which fits the experimental data reasonably well, but fails to accurately describe the steep portion of the deliquescence branch. The dark blue curves indicate a fully kinetic simulation with ResAM, which shows that only taking the slow diffusive processes into account provides full overlap with measurements during the two hours long deliquescence process.

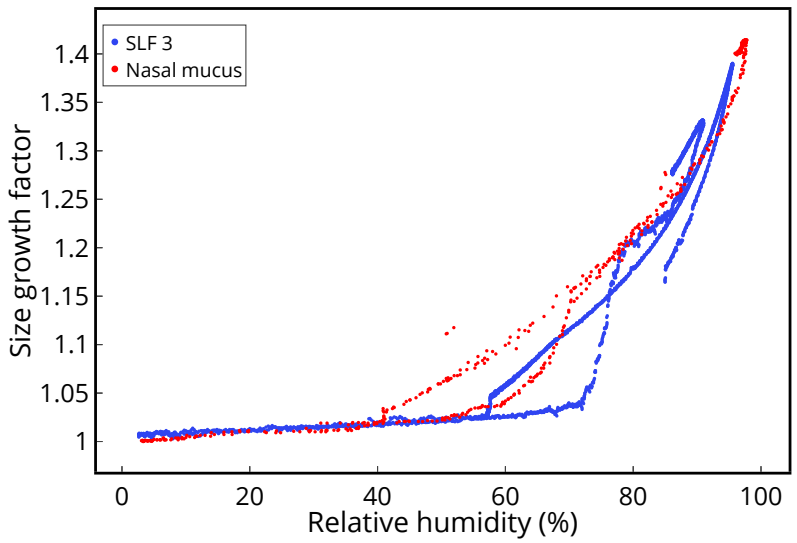

Fig. S5. Size growth factor of SLF and nasal mucus. Mie-Resonance spectra (49, 50) of two selected EDB measurements of SLF (blue data points, particle SLF 3 in Fig. S4) and nasal mucus (red data points) have been normalized to show the size growth factor as function of RH. Size growth at RH $>$ 80% is similar for both particles, but efflorescence and deliquescence RHs differ. For SLF particles, salt effloresces at $\sim$ 56% RH, whilst the nasal mucus particle effloresces only at 42% RH. In addition, deliquescence occurs in SLF around 75% RH, similar to aqueous NaCl, whereas nasal mucus deliquesces at RH $\sim$ 69%. This indicates that SLF particles are dominated by NaCl, whereas the nasal mucus contains significant amounts of other salts.

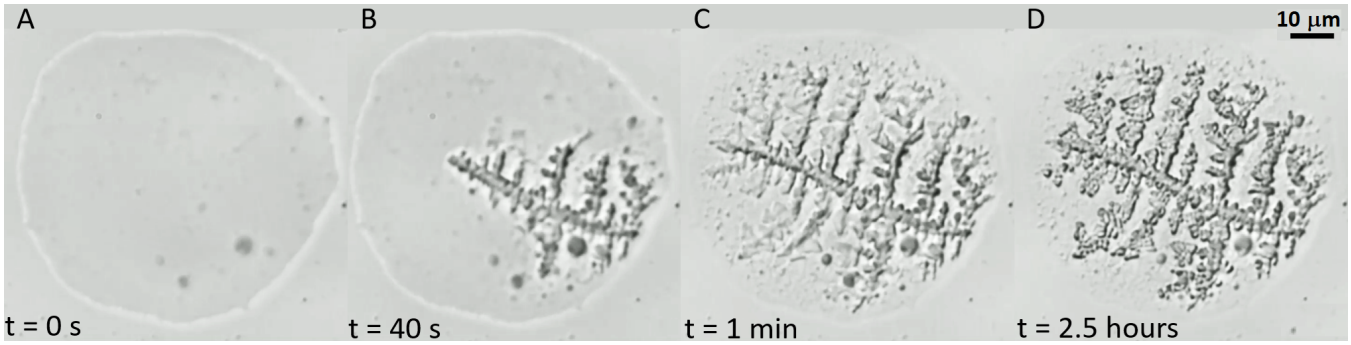

Fig. S6. Time series of microscope images (50x) of an efflorescing synthetic lung fluid (SLF) particle deposited on a hydrophobically coated substrate in a temperature and humidity controlled cell. The setup is described in detail by Ciobanu et al. (52). At 20.5°C and 54% relative humidity the particle's radius is approximately 40 µm (scalebar represents 10 µm). (**A**) Liquid particle at $t = 0$, when efflorescence begins. (**B**) 40 s after the start of crystallization with rapid dendritic NaCl crystal growth. (**C**) 1 min after initial crystallization the crystal reaches the edge of the droplet, slowing the speed of further crystallization dramatically. (**D**) 2.5 h after initial crystallization the crystal is still growing slowly, leading to a coarsening of the crystal structure. The size of the dendrites is used to calculate the morphology-dependent effective diffusion constant of Na^+ and Cl^- ions in the remaining, mainly organic solution (see section "Boundary condition at the liquid-solid interface and dendritic crystal growth habit").

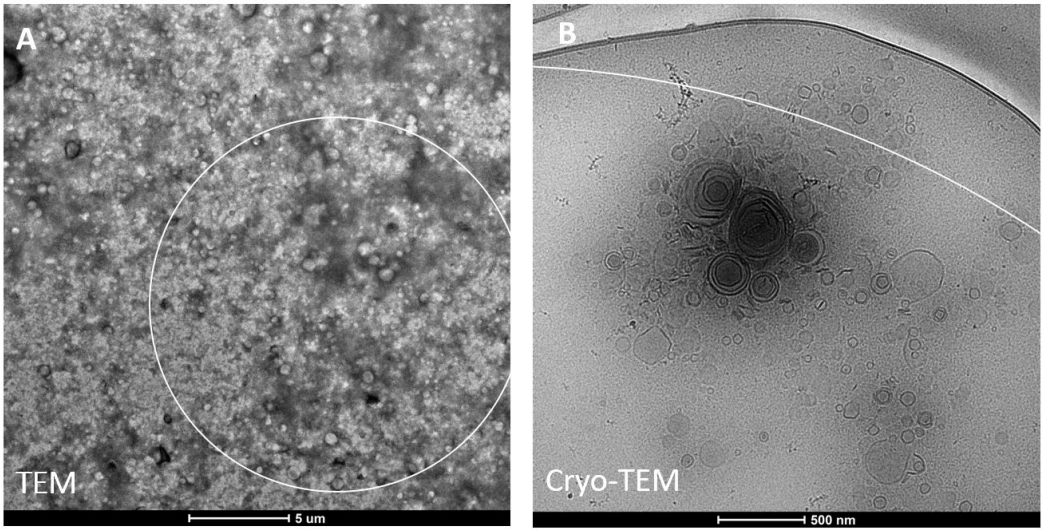

Fig. S7. Microstructures in synthetic lung fluid (SLF). The structure of SLF was investigated using (**A**) TEM and (**B**) cryo-TEM. SLF exhibits a colloidal structure, possessing vesicles similar in nature to those found in lung fluid extracts (53). DLS measurements of the particles in SLF showed that the particles have an average particle size of 124 nm, but ranged from 59 nm to 220 nm. The size of liposomes influences the size of particles in the SLF solution. For comparison with the shown inhomogeneities, the white circles indicate typical sizes of particles investigated in the EDB in the present work.

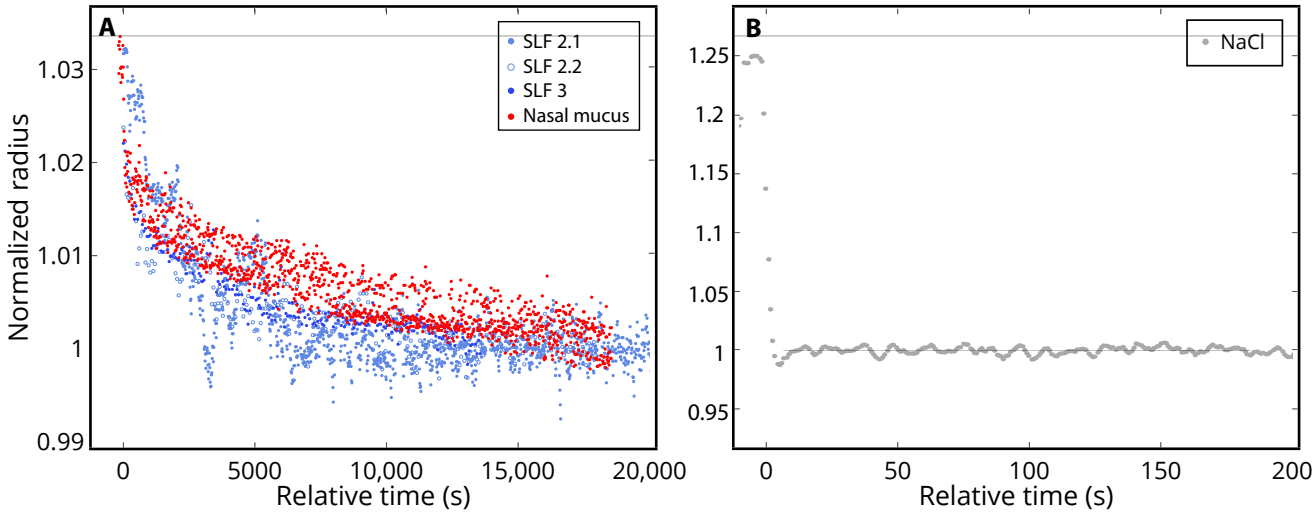

Fig. S8. Second kinetically impeded stage of efflorescence after the initial rapid first stage of two different SLF particles and one nasal mucus particle. For comparison, an NaCl particle displays only a single efflorescence stage. (**A**) Similar to Fig. 2B, but focusing on the slow crystal growth stage after the initial fast loss of water. In contrast to Fig. 2B, here the data is obtained from the Mie-Resonance spectra, providing a more accurate (though also much more elaborate) determination of radius than voltage does (49, 50). Light blue symbols show two different efflorescence cycles of particle SLF 2 (labelled as SLF 2.1 and 2.2). Dark blue symbols show measurements for particle SLF 3. Red symbols indicate measurements for a nasal mucus particle. These independent spectroscopic data do not only corroborate the voltage data showing kinetically impeded water loss, but they confirm reproducibility. Most importantly, nasal mucus shows a similar behavior to SLF, i.e. this is not a unique property of SLF. An exponential curve was fitted to these data sets and characteristic times were calculated as: 1500 s (SLF 2.1), 3000 s (SLF 2.2), 1700 s (SLF 3), and 2800 s (nasal mucus). (**B**) Efflorescence of a NaCl particle for comparison (voltage measurements by Braun et al. (54) converted to normalized radius). The NaCl particle loses water almost instantaneously and equilibrates with the environment within a few seconds. Note that the radius cannot be obtained for NaCl particles after efflorescence due to their non-sphericity, therefore voltage data have to be used.

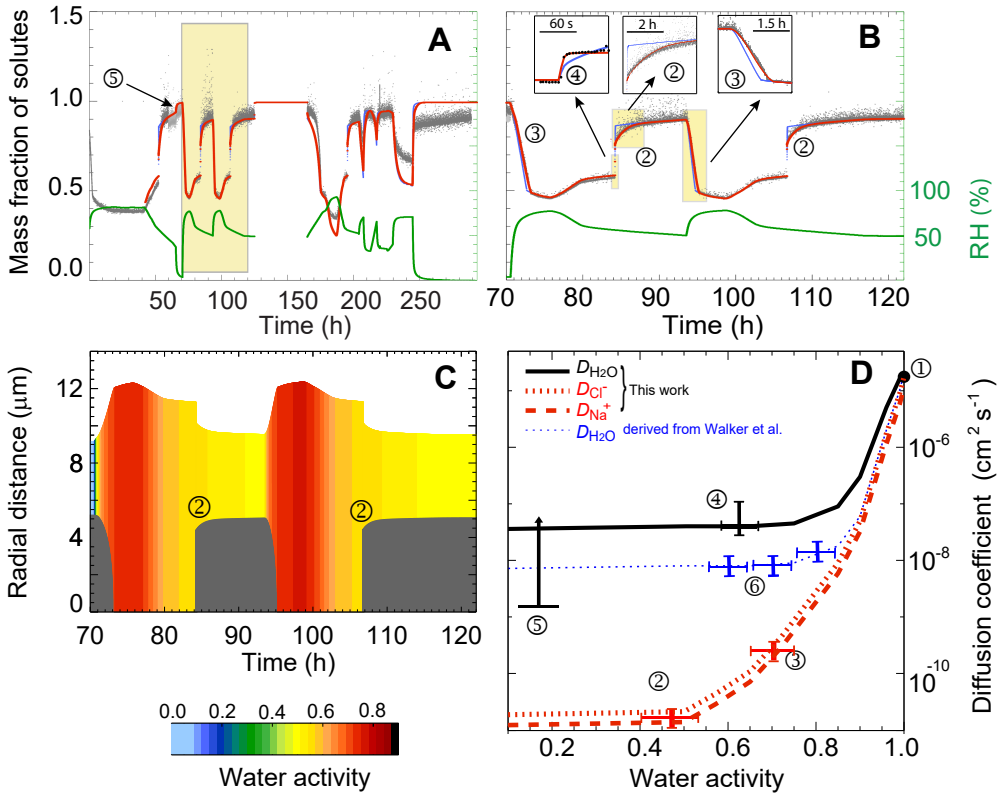

Fig. S9. Measured and modeled deliquescence/efflorescence cycles of a synthetic lung fluid (SLF) particle levitated in an electrodynamic balance (EDB) and forced by prescribed changes in relative humidity (RH). (**A**) Similar to Fig. 2, but showing mass fraction of solute (grey dots) instead of voltage, along with prescribed relative humidity, RH (green curve) and ResAM results (red curve). Full 12-day measurement of SLF particle with a dry radius R of $\sim$ 9.7 µm undergoing four efflorescence/deliquescence cycles. Cycle 1 (40-70 h) was used for instrument tuning and camera adjustments. Cycles 2+3 (highlighted in yellow) were used to derive the liquid phase diffusion constants of water molecules and Na^+ and Cl^- ions, D_{ℓ,H_2O} and $D_{\ell,ions}$. The period 125-165 h was used to perform independent measurements of the drag force on the particle induced by the gas flow (not shown). Cycle 4 yielded mass fractions of solutes and diffusivities similar to the previous Cycles 2 and 3. (**B**) Zoom on the highlighted Cycles 2+3, showing fast initial crystal growth and loss of water $\sim$ 4 s after efflorescence, followed much by slower ($\Delta t \sim$ hours) crystal growth caused by Na^+ and Cl^- ions diffusing to the crystal through liquid of progressively increasing viscosity, with a diffusion constant $D_{\ell,ions} \approx R^2/\Delta t \approx 10^{-10}$ cm^2/s. Red and blue curves in the small inserts show the results of the respiratory aerosol model ResAM: the red curve indicates the fully fitted model with $D_{\ell,ions} \ll D_{\ell,H_2O}$ (see black and red curves in panel D for final fits of diffusivities), whilst the blue curve assumes all diffusivities to be identical ($D_{\ell,ions} = D_{\ell,H_2O}$) and to follow the blue line in panel D. (**C**) Modeled water activity and NaCl crystal growth (dark grey cores) in the particle during the humidification cycles highlighted in yellow in panel A. (**D**) Diffusion coefficients for H_2O, Na^+ and Cl^- as derived from the measurements (circled numbers refer to the times marked with the same numbers in panels A-C). The black curve indicates D_{ℓ,H_2O} in SLF. The red curves indicate $D_{\ell,ions}$ (with $D_{\ell,Cl^-} \sim 1.4 \times D_{\ell,Na^+}$, see section "Liquid phase diffusion"). The blue curve is an estimate of D_{ℓ,H_2O} derived by ResAM from measurements in SLF by Walker et al. (51), which is about a factor of five smaller than our present study, possibly due to composition inhomogeneities of SLF (see Fig. S4A), but by more than a factor of 100 larger than the ion diffusivities in the present study (so that aerosol modeling using only the Walker data would lead to an overestimation of virus inactivation).

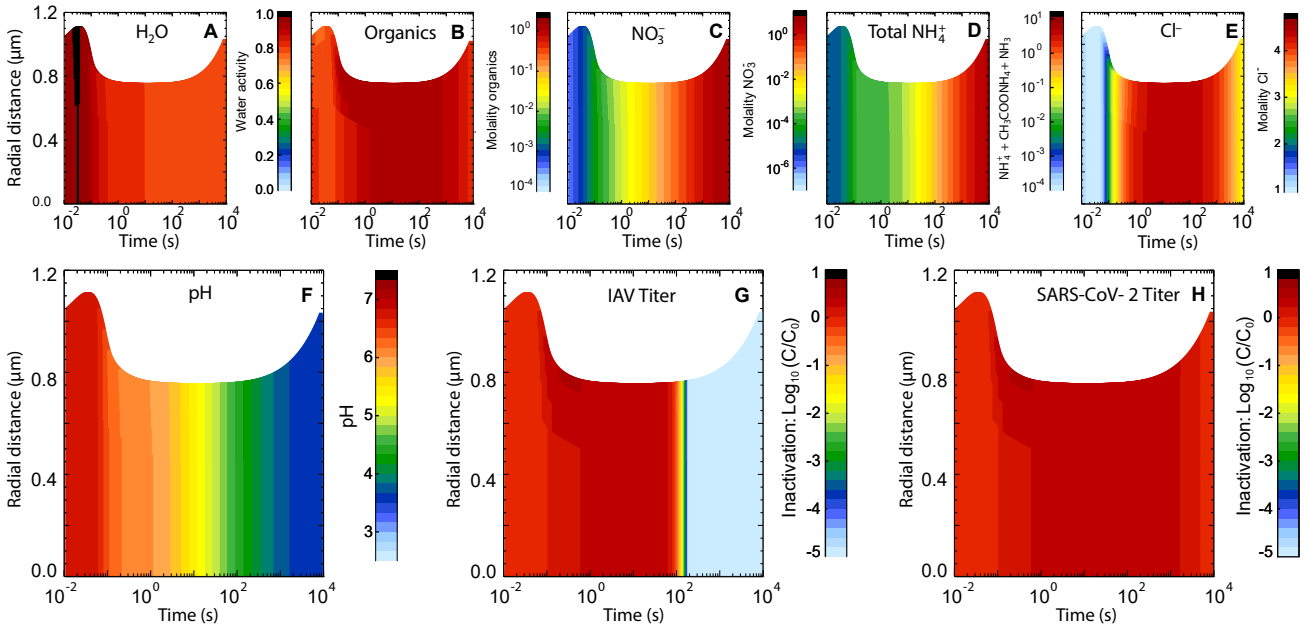

Fig. S10. Evolution of physicochemical conditions within a respiratory particle and concomitant inactivation of viruses trapped in the particle during transition from nasal to humid indoor air conditions, modeled with ResAM. Same as Fig. 3 but for 80% RH. As a consequence of the higher RH, the particle shrinks less, concentrations of all chemical species stay lower, and the salt does not effloresce. However, overall the evolution of pH is not very different upon exhalation, leading to an inactivation time of $\sim$ 2.5 minutes for influenza virus at 80% RH compared to $\sim$ 3 minutes at 50% RH. In either case, coronaviruses remain active.

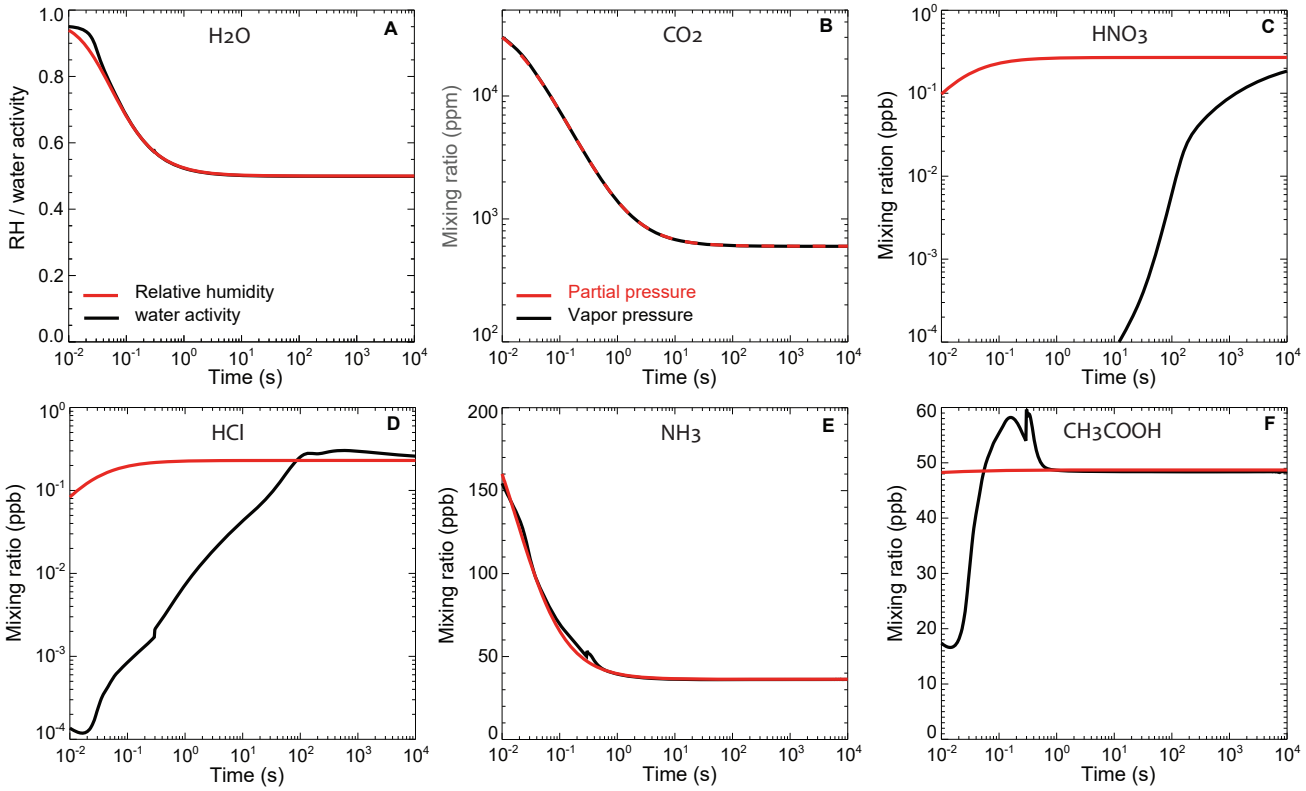

Fig. S11. Non-equilibrium conditions of chemical species in the gas phase above expiratory particle surface leading to their growth or evaporation. Relative humidity and mixing ratios (or mole fractions) of gaseous species in the exhaled plume mixing with ambient air (red lines) in comparison with equilibrium values corresponding to the vapor pressures of the exhaled particles (black lines) for typical indoor air simulations shown in Fig. 3. Panel (**A**) shows relative humidity and water activity of the outermost shell; panels (**B**) to (**F**) show CO_2, HNO_3, HCl, NH_3, and CH_3COOH. The difference between the red and black lines represents the force on the particles, i.e. supersaturation and uptake of the gaseous species when the red values are higher, subsaturation and loss of the species to the gas phase when the black values are higher.

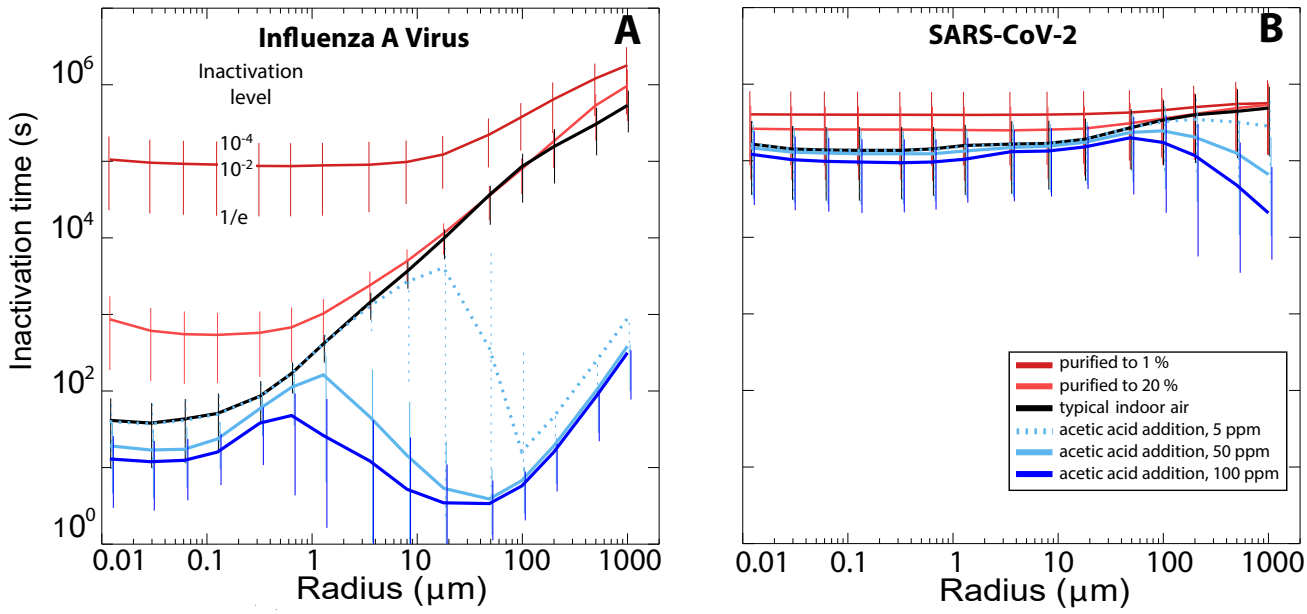

Fig. S12. Modeled inactivation times for IAV and SARS-CoV-2 as a function of particle size when adding acetic acid to indoor air. Inactivation times for (**A**) IAV, and (**B**) SARS-CoV-2, when expelled into typical room air (black curve), indoor air purified to 20% (orange curve) or 1% (red curve), or indoor air supplemented with 5 ppm (dotted light blue curve), 50 ppm (solid light blue curve) or 100 ppm (dark blue curve) acetic acid. The exposure threshold of acetic acid is 10 ppm averaged over an 8-hour work shift. Enrichment of acetic acid in indoor air within this acceptable range cannot achieve a sufficient reduction in particle pH and, therefore, yields no robust reduction in virus inactivation times (except for large particles, in which very low pH (< 2.5) can be achieved due to much higher gas phase concentration of CH_3COOH than NH_3 and the faster liquid diffusivity of undissociated CH_3COOH molecules than NH_4^+ ions).

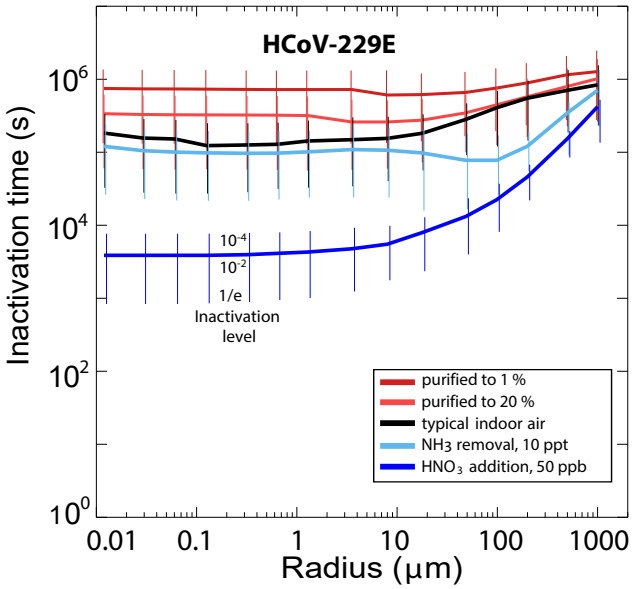

Fig. S13. Inactivation time for HCoV-229E as function of particle radius and air composition. Analogous to 4D-E. Indoor air with typical composition (black), enriched to 10 or 50 ppb HNO_3 (blue), or purified air with HNO_3 and NH_3 reduced to 20% or 1% (red). Whiskers show reductions of virus load to 10^{-4} (upper end), 10^{-2} (intersection with line) and 1/e (lower end). The gas phase compositions of exhaled air and the various cases of indoor air are defined in Table S4. The exhaled air is assumed to mix with the indoor air by a turbulent eddy diffusion coefficient of 50 $cm^2\ s^{-1}$. Radius values refer to the particle size 1 s after exhalation.

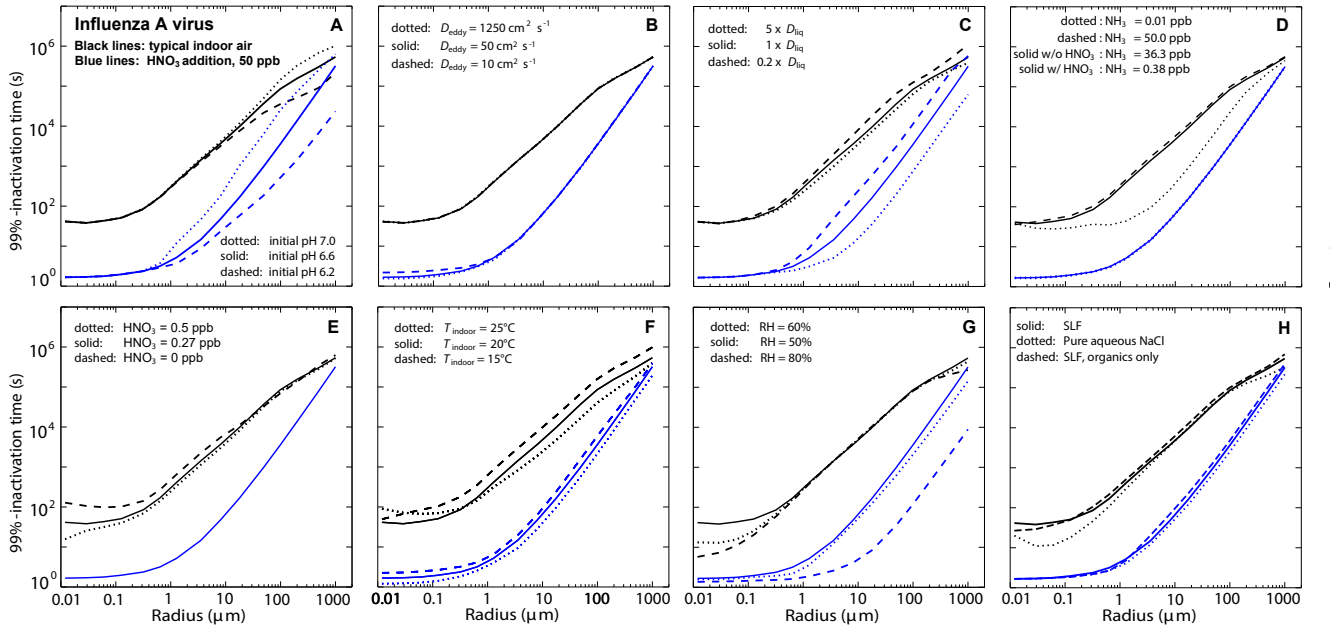

Fig. S14. Sensitivity studies for the inactivation of IAV. In each panel, black lines indicate typical (untreated) indoor air, and blue lines indicate typical indoor air enriched to 50 ppb HNO_3. (**A**) Sensitivity to buffering as expressed by initial exhaled particle pH varying from 6.2 to 7.0 (see section "Aerosol initial pH buffering" for details). (**B**) Sensitivity to mixing speed of exhalation plume with indoor air, expressed by an eddy diffusion coefficient (see Eq. S25), which is characteristic for a given ventilation (air change per hour, ACH). The highest eddy diffusion coefficient 1250 cm^2s^{-1} applies to ACH = 10, 50 cm^2s^{-1} to ACH = 2 and 10 cm^2s^{-1} to ACH = 0.1. (**C**) Sensitivity to uncertainties in the liquid phase diffusion coefficients (increasing or decreasing by a factor of 5). (**D**) Sensitivity to indoor ammonia concentrations varying from conditions in a clean room (0.01 ppb) to conditions in a polluted house or nursing home (50 ppb)(35). (**E**) Sensitivity to indoor gaseous nitric acid concentrations varying from conditions found in libraries and museums (0.0 ppb) to conditions of the highest indoor values in houses with natural ventilation (0.5 ppb)(35). (**F**) Sensitivity to indoor temperature (15-25°C), applying the temperature dependencies of all physicochemical parameters and assuming the virus inactivation rates to increase by a factor of 1.5 when temperature is increased by 5°C (conservatively estimated based on results in (39)). (**G**) Sensitivity to indoor relative humidity (with 40% RH values obtained from linear extrapolation of all parameters between 60% and 50%, i.e. with high uncertainty). (**H**) Sensitivity to exhaled aerosol composition, namely reducing composition to only the organic components of SLF (dashed line) or pure NaCl (dotted line).

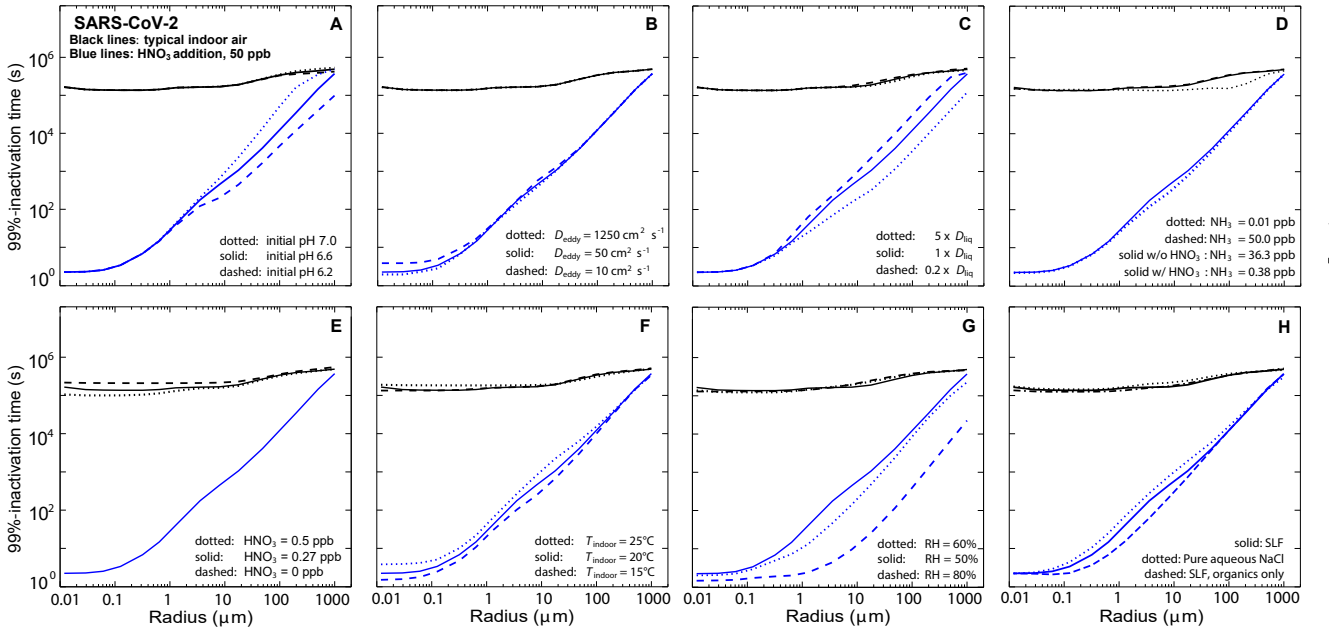

Fig. S15. Sensitivity studies for the inactivation of SARS-CoV-2. Same sensitivity tests as in Fig. S14, but for SARS-CoV-2 instead IAV. For Panel **F**, the virus inactivation rates are assumed to increase by a factor of 1.3 when temperature is increased 5°C (following (55)).

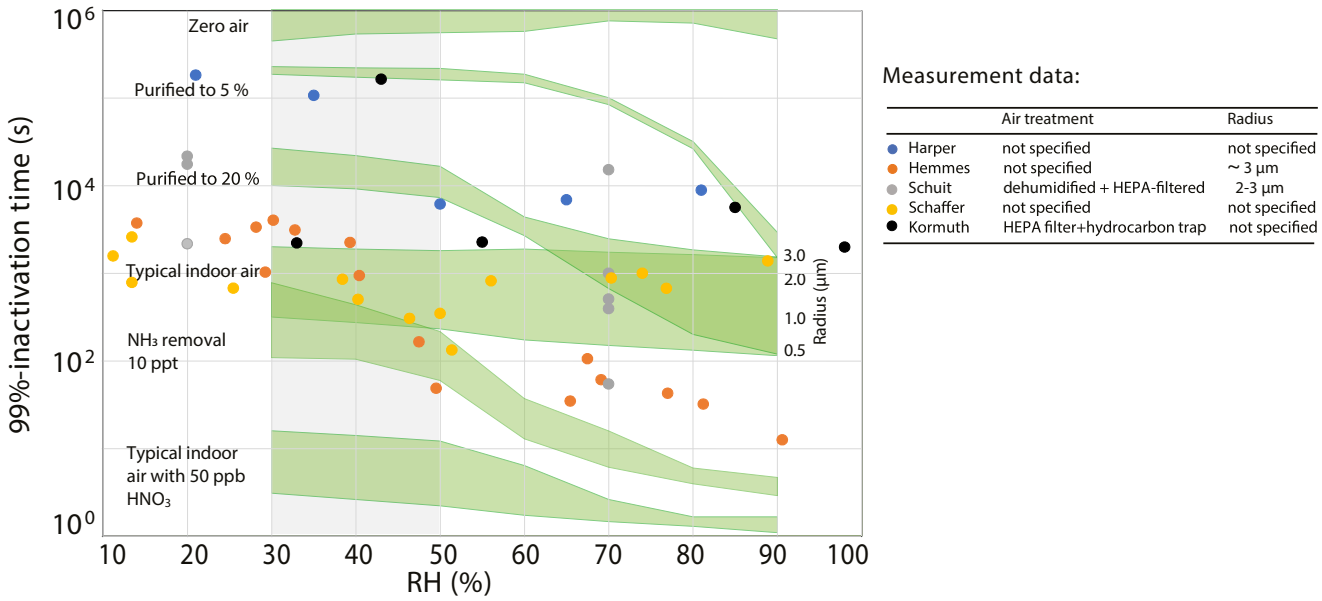

Fig. S16. Comparison of measured 99%-inactivation times of IAV in aerosols with modeled inactivation for different compositions of air (shaded in green). Colored circles refer to measurements based on the literature sources listed in the accompanying table (all obtained experimentally at temperatures between 20-25°C). Aerosol particle sizes reported in the literature are typically a few micrometers, but often not specified. Air treatment in the published aerosol experiments, where stated, includes HEPA-filtering and other air purification measures. Such treatments partly remove pH-relevant species from the air, such as HNO_3, which increases the aerosol pH (partly compensated by a reduced concentration of NH_3). Inactivation times were estimated assuming first-order kinetics, and were calculated from inactivation rate constants, half lives or decay curve data shown in the publications. Areas highlighted in green refer to ResAM model results with aerosol particle radii ranging from 0.5 µm to 3 µm (as indicated at their right end). The inactivation rate itself is a function of time due to the dependence on the changing pH. This implies that cases with 99%-inactivation times of many hours or days are only inaccurately determined by the measurements, which typically last for only about an hour; therefore we constrained the model results to the duration of the experiment and extrapolated the results to achieve measurement-model comparability. The composition of indoor air with and without various treatments used in ResAM is given in Table S4. Model results in the range 30-50% RH are very uncertain and therefore grayed out. Citations refer to: Harper (39); Hemmes (56); Schuit (44); Schaffer (57); Kormuth (43). Overlapping data points were slightly shifted in RH for clarity.

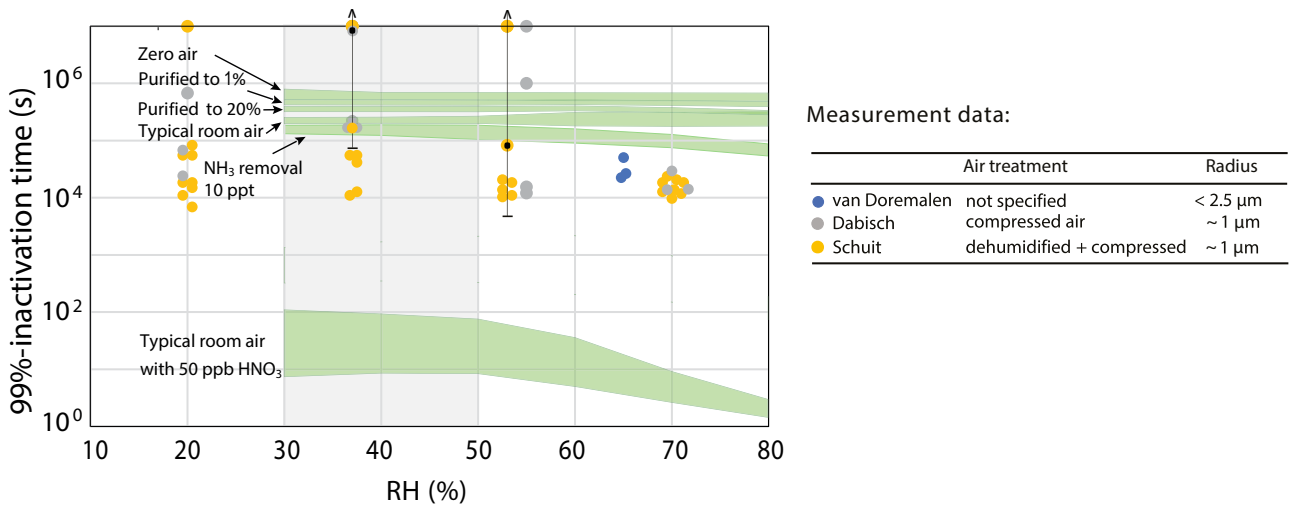

Fig. S17. Comparison of measured 99%-inactivation time of SARS-CoV-2 with modelled inactivation for different composition of air (shaded in green). Colored circles refer to measurements based on the literature sources listed in the accompanying table (all obtained experimentally at temperatures between 20-23°C). Aside from controlling temperature and RH, air treatment in the published aerosol experiments was not specified, and the air composition under which inactivation data were obtained is therefore unknown. Inactivation times were estimated assuming first-order kinetics, and were calculated from inactivation rate constants or decay curve data shown in the publications. Note that Schuit *et al.* and Dabisch *et al.* also measured inactivation under the influence of solar irradiance, resulting in shorter inactivation times ($\sim 10^3$ s) than the dark inactivation measurements shown here. Measurement variability among experimental replicates is large, in particular at inactivation times larger than one day ($\sim 10^5$ s), as indicated by the arrow shown in two examples. Areas highlighted in green refer to ResAM model results with aerosol particle radii ranging from 0.5 µm to 3 µm. The inactivation rate itself is a function of time due to the dependence on the changing pH. This implies that cases with 99%-inactivation times of many hours or days are only inaccurately determined by the measurements, which typically last for only one to three hours; therefore we constrained the model results to the duration of the experiment and extrapolated the results to achieve measurement-model comparability. The composition of indoor air with and without various treatments used in ResAM is given in Table S4. Model results in the range 30-50% RH are very uncertain and therefore grayed out. Citations refer to: van Doremalen (58); Dabisch (55); Schuit (59). Overlapping data points were slightly shifted in RH for clarity.

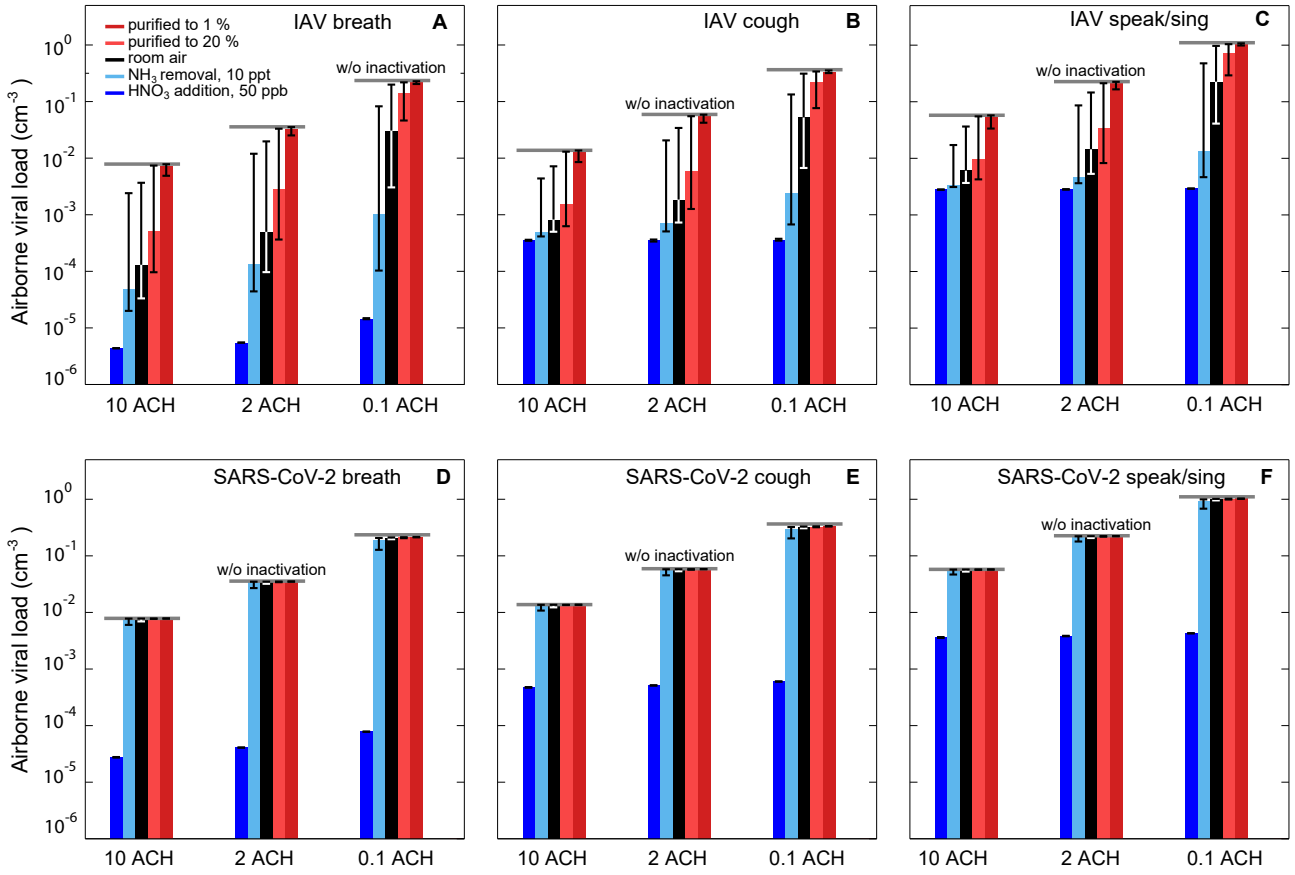

Fig. S18. Airborne viral load under steady state conditions assuming that the number of viruses per aerosol particle increases with particle size (rather than assuming one virus per particle irrespective of size, as in Fig. 5). Specifically, we assume that the virus concentration in the particles is proportional to their radius, as motivated by data assembled by Pöhlker et al. (37). Like in Fig. 5, the steady state conditions are calculated assuming one infected person per 10 m^3 of air volume, emitting the virus-laden aerosol, which is balanced by aerosol removal via ventilation and deposition, as well as by pH-moderated virus inactivation. The air is subject to different ventilation strengths (Air Change per Hour, ACH) and different air treatments (colored bars, see legend in panel A) for various human activities. These activities include normal breathing, coughing, and speaking/singing, leading to the exhalation of different sizes of aerosol particles (see Fig. 4E and Ref. (37)). Upper row (**A**-**C**) shows results for IAV, lower row (**D**-**F**) for SARS-CoV-2. The left column (**A**, **D**) shows results for normal breathing; the center column (**B**, **D**) for coughing; and the right column (**C**, **F**) for speaking or singing.

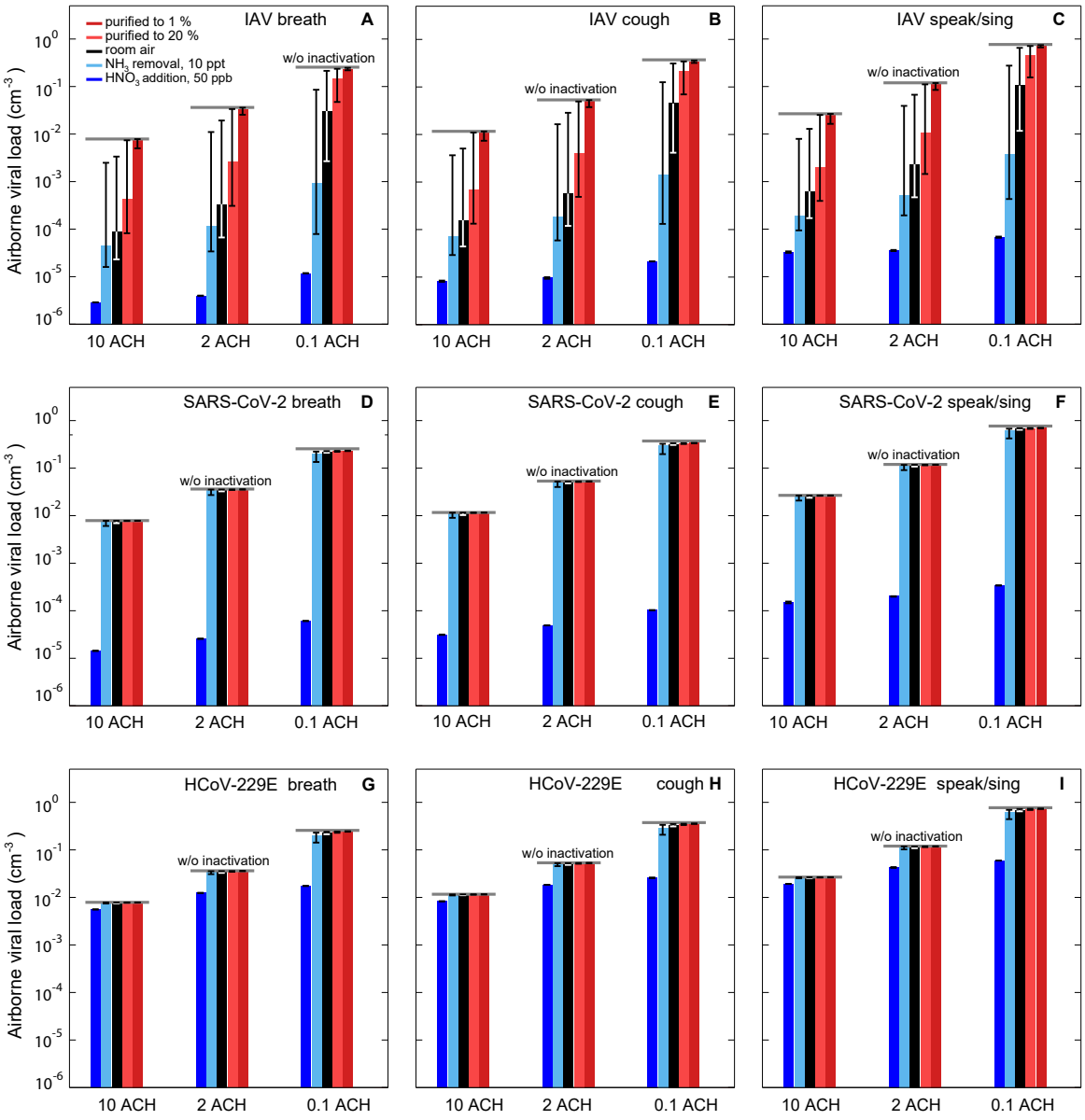

Fig. S19. Airborne viral load under steady state conditions for IAV, SARS-CoV-2 and HCoV-229E at different ACH and different room conditions for breathing, coughing, and speaking/singing. Same as Fig. S18 but assuming one virus per aerosol particle, irrespective of radius, and including results for HCoV-229E in the bottom row (**G-I**). For a detailed description see Fig. 5 and section "Modeling of indoor airborne viral load and relative risks of transmission".

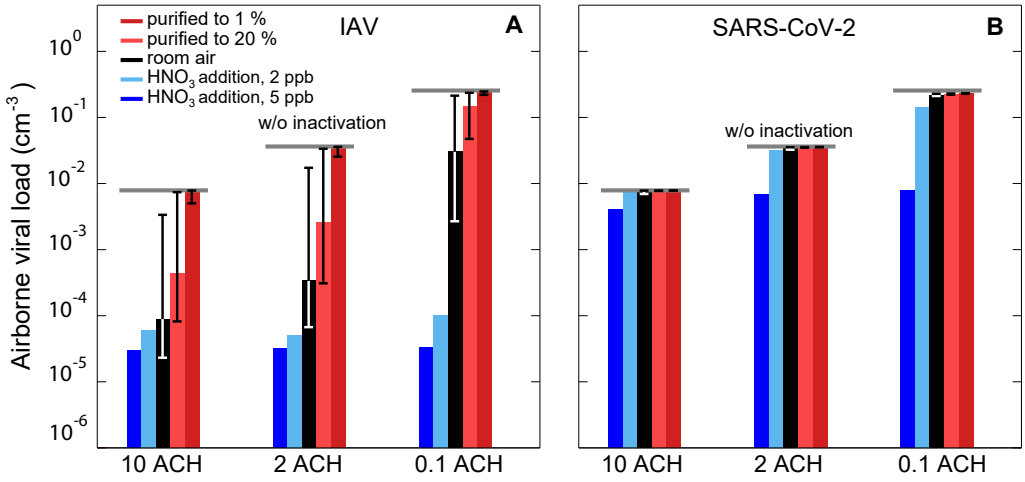

Fig. S20. Airborne viral load under steady state conditions for IAV and SARS-CoV-2, specifically for air treatment applying low HNO_3 concentrations. Same as Fig. S19A+D, but using only 2 and 5 ppb HNO_3 to acidify the indoor air.

Supporting Tables

Table S1. Composition of the synthetic lung fluid (SLF), adapted from Bicer (4)

Components	Concentration (mass per volume of solution)
Solvent	
Water	-
Salts	
Calcium chloride dihydrate	0.185 mg/ml
Magnesium sulfate heptahydrate	0.200 mg/ml
Potassium chloride	0.400 mg/ml
Potassium phosphate monobasic anhydrous	0.060 mg/ml
Sodium bicarbonate	0.350 mg/ml
Sodium chloride	8.000 mg/ml
Sodium phosphate dibasic heptahydrate	0.090 mg/ml
Sugars	
Dextrose anhydrous	1.000 mg/ml
Proteins	
Albumin	8.800 mg/ml
Transferrin	1.500 mg/ml
Lipids	
DPPC	4.800 mg/ml
DPPG	0.500 mg/ml
Cholesterol	0.100 mg/ml
Antioxidants	
Ascorbic acid	0.025 mg/ml
Uric acid	0.016 mg/ml
GSH (glutathione)	0.052 mg/ml

Table S2. Equilibrium constants used for the kinetic simulations. They are valid for environment temperature from 0°C to 40°C.

Reaction			Equilibrium constant	Unit	Source
$H_2O_{(aq)}$	$\rightleftharpoons$	$H_2O_{(gas)}$	$p_{H_2O} = a_w \times p_{\text{pure water}}$,[a]	Pa	(18, 19, 34)
$H_2O_{(aq)}$	$\rightleftharpoons$	$H^+ + OH^-$	$\exp\left(-9.2644 - \frac{6872.7}{T}\right)$	molality^2	(60)
$H^+ + NH_{3(gas)}$	$\rightleftharpoons$	NH_4^+	$\exp\left(-5.2167 + \frac{9826.67}{T} - 0.00787 \times T\right)$	atm^{-1}	(61)
$CH_3COOH_{(gas)}$	$\rightleftharpoons$	$CH_3COOH_{(aq)}$	$4000 \times \exp\left(6200(\frac{1}{T} - \frac{1}{298.15})\right)$	molality atm^{-1}	(62)
$CH_3COOH_{(aq)}$	$\rightleftharpoons$	$H^+ + CH_3COO^-$	[b]	molality	(63)
$HCl_{(gas)}$	$\rightleftharpoons$	$H^+ + Cl^-$	[c]	molality^{2}atm^{-1}	(18, 19)
$HNO_{3(gas)}$	$\rightleftharpoons$	$H^+ + NO_3^-$	[d]	molality^{2}atm^{-1}	(18, 19)
$CO_{2(aq)} + H_2O_{(aq)}$	$\rightleftharpoons$	$H^+_{(aq)} + HCO_3^-$(aq)	$4.448 \times 10^{-7} \exp(-2133(\frac{1}{T} - \frac{1}{298.15}))$	molality	(64, 65)
$HCO_3^-{}_{(aq)}$	$\rightleftharpoons$	$H^+_{(aq)} + CO_3^{-2}$(aq)	$1.08555 \times 10^{-9} \exp(-3347.3(\frac{1}{T} - \frac{1}{298.15}))$	molality	(65)
$CO_{2(gas)}$	$\rightleftharpoons$	$CO_{2(aq)}$	$0.034 \times \exp\left(2300(\frac{1}{T} - \frac{1}{298.15})\right)$	molality atm^{-1}	(62)
$NH_4CH_3COO_{(ad)}$	$\rightleftharpoons$	$NH_4^+{}_{(aq)} + CH_3COO^-{}_{(aq)}$	3.44×10^{-3} at $T = 293.55$ K only	molality	[e]
$NaCl_{(solid)}$	$\rightleftharpoons$	$Na^+ + Cl^-$	$13.812 - 0.025681 \times (T - 298.15)$	molality^2	[f]

[a] $p_{\text{pure water}}$ is given by Eq. 11 of Murphy and Koop (34)

[b] $\log K = -1500.65/T - 6.50923 \log T - 0.0076792 \times T$

[c] $\ln K = 14.53335 + 3067.38(1/T - 1/298.15) - 19.91 \ln(T/298.15)$

[d] $\ln K = 394.007 - 3020.3522/T - 71.002 \ln(T) + 0.131442311 \times T - 0.420928363 \times 10^{-4} \times T^2$.

[e] The dissociation coefficient of NH_4CH_3COO is estimated from our own measurement of NH_3 vapor which is 0.12 Pa at $T = 293.55$ K and RH of 87.5%.

[f] The activity product of solid NaCl is calculated with ResAM using the NaCl solubility data in water (66).

Table S3. Liquid phase diffusion coefficients of chemical species relevant in expiratory aerosol particles in infinitely diluted water at 298.15 K.

Species	D_ℓ in 10^{-5} cm^{2}s^{-1}	Source	Species	D_ℓ in 10^{-5} cm^{2}s^{-1}	Source
H_2O	2.44	(67)	NH_3	1.7	(68)
H^+	9.3	(67)	NH_4^+	1.7	(69)
Na^+	1.33	(67)	CH_3COOH	1.18	(22)
Cl^-	2.03	(67)	CH_3COO^-	1.08	(22)
NO_3^-	1.90	(67)	NH_4CH_3COO	1.18	*a*
OH^-	5.25	(67)	CO_2	1.98	(68)
Proteins/lipids	0	*b*	HCO_3^-	1.11	(68)

[a] We assume the molecular form of ammonium acetate, NH_4CH_3COO, to have the same diffusion coefficient as CH_3COOH.

[b] The liquid phase diffusion of lipids and proteins is assumed to be extremely slow and can be ignored.

Table S4. Trace gases in exhaled air and in indoor air for different scenarios. In the present study, we assume the relative humidity of the indoor air to be 50 % and the temperature 293.15 K, unless stated differently (e.g., Fig. S10, Figs. S14E,G and S15E,G). The background aerosol loading is assumed to be 20 µg/m^3. The temperature of exhaled air at time zero is assumed to be 307.15 K (31). The entries with enriched acetic acid (CH_3COOH) serve as basis for Fig. S12. The gas phase concentrations in this table apply to normal ventilation, ACH of $\approx$ 2.

Scenario	RH	NH_3/ppb	HNO_3/ppb	HCl/ppb	CH_3COOH/ppb	CO_2/ppm
		Mean (UL|LL)*	Mean (UL|LL)	Mean (UL|LL)	Mean (UL|LL)	Mean (UL|LL)
exhaled air	91%[a]	238 (738|38) [b]	0.0[c]	0.0[c]	486(70, 71)	46,500[d]
Typical indoor air	50%	36.3 (61|8.1) [e]	0.27 (0.84|0.029) [f]	0.237 (0.85|0)(35)	48.7 (170|10.82)(35)	600(35)
Purified indoor air to 20%	50%	7.26 (12.2|1.62)	0.054 (0.164|0.0058)	0.0474 (0.17|0)	9.74 (34|2.164)	600
Purified indoor air to 1%	50%	0.363 (0.61|0.081)	0.0027 (0.0082|0.00029)	0.00237 (0.0085|0)	0.487 (1.70|0.1082)	600
Zero air	50%	0	0	0	0	600
Indoor air, NH_3 removal	50%	0.01[g]	0.42 (1.62|0.0415) [h]	0.237 (0.85|0)	48.7(170|10.82)	600
Indoor air with 50 ppb HNO_3	50%	0.376[g]	50	0.237 (0.85|0)	48.7 (170|10.82)	600
Indoor air with 5 ppm CH_3COOH	50%	35.8[g]	0.27	0.237	5×10^3	600
Indoor air with 50 ppm CH_3COOH	50%	18.47[g]	0.293	0.237	50×10^3	600
Indoor air with 100 ppm CH_3COOH	50%	11.10[g]	0.43	0.237	100×10^3	600

* UL: Upper limit, LL: Lower limit

[a] Berry reported a H_2O amount in exhaled air of 0.0342 grams per liter (31). A relative humidity of 91% is obtained using the vapor pressure expression of Murphy and Koop (34) at exhalation temperature.

[b] See Nazaroff and Weschler (35), page 575.

[c] There are no literature values for HCl and HNO_3 concentrations in exhaled air. Thus, we assume they are zero.

[d] CO_2 concentration in exhaled air is $(46.5\pm6.5)\times10^3$ ppm (72).

[e] Weighted average, maximum, and minimum of all indoor values in Table 6 of Nazaroff and Weschler (35).

[f] Weighted average, maximum, and minimum of all indoor values with natural ventilation or window air conditioners in Table 12 of Nazaroff and Weschler (35).

[g] When adding HNO_3 to indoor air, ammonia is reduced due to the uptake by the background aerosol. Prior to the addition, the indoor air is assumed to have a loading of 20 µg/m^3. The molalities of indoor background aerosol (with water activity of 0.5 corresponding to 50% RH) are: 6.36 mol/kg sucrose, 6.36 mol/kg sulfate ions, 23.89 mol/kg NH_4^+, and 11.16 mol/kg NO_3^- .

[h] When NH_3 is scrubbed from the indoor air while the particulate matter is not removed, the ammonium (NH_4^+) in the background particles will partition to the gas phase. This results in the release of HNO_3 to the gas phase from the nitrate (NO_3^-) in the particular matter, enhancing the virus inactivation. The lower HNO_3 limit specified here refers to zero NO_3^- in the background aerosol and the upper limit to 40 nmol/m^3 NO_3^-, as summarized by (35).

References

1. van den Worm, S. H. E.; Eriksson, K. K.; Zevenhoven, J. C.; Weber, F.; Züst, R.; Kuri, T.; Dijkman, R.; Chang, G.; Siddell, S. G.; Snijder, E. J.; Thiel, V.; Davidson, A. D., Reverse genetics of SARS-related coronavirus using vaccinia virus-based recombination. *PLoS ONE* **7**, e32857 (2012).
2. Wölfel, R.; Corman, V. M.; Guggemos, W.; Seilmaier, M.; Zange, S.; Müller, M. A.; Niemeyer, D.; Jones, T. C.; Vollmar, P.; Rothe, C.; Hoelscher, M.; Bleicker, T.; Brünink, S.; Schneider, J.; Ehmann, R.; Zwirglmaier, K.; Drosten, C.; Wendtner, C., Virological assessment of hospitalized patients with COVID-2019. *Nature* **581**, 465–469 (2020).
3. Spieler, E. E.; Moritz, E.; Stertz, S.; Hale, B. G., Application of a biologically contained reporter system to study gain-of-function H5N1 influenza A viruses with pandemic potential. *mSphere* **5**, e00423–20 (2020).
4. Bicer, E. M., Ph.D. thesis (King's College London) (2014).
5. Hassoun, M.; Royall, P. G.; Parry, M.; Harvey, R. D.; Forbes, B., Design and development of a biorelevant simulated human lung fluid. *J. Drug Deliv. Sci. Technol.* **47**, 485–491 (2018).
6. Busnadiego, I.; Fernbach, S.; Pohl, M. O.; Karakus, U.; Huber, M.; Trkola, A.; Stertz, S.; Hale, B. G., Antiviral activity of type I, II, and III interferons counterbalances ACE2 inducibility and restricts SARS-CoV-2. *mBio* **11**, e01928–20 (2020).
7. Davis, E. J.; Buehler, M. F.; Ward, T. L., The double-ring electrodynamic balance for microparticle characterization. *Rev. Sci. Instruments* **61**, 1281–1288 (1990).
8. Colberg, C. A.; Krieger, U. K.; Peter, T., Morphological investigations of single levitated $H_2SO_4/NH_3/H_2O$ aerosol particles during deliquescence/efflorescence experiments. *J. Phys. Chem. A* **108**, 2700–2709 (2004).
9. Steimer, S. S.; Krieger, U. K.; Te, Y. F.; Lienhard, D. M.; Huisman, A. J.; Luo, B. P.; Ammann, M.; Peter, T., Electrodynamic balance measurements of thermodynamic, kinetic, and optical aerosol properties inaccessible to bulk methods. *Atmospheric Meas. Tech.* **8**, 2397–2408 (2015).
10. Haddrell, A. E.; Davies, J. F.; Yabushita, A.; Reid, J. P., Accounting for changes in particle charge, dry mass and composition occurring during studies of single levitated particles. *J. Phys. Chem. A* **116**, 9941–9953 (2012).
11. Tang, I. N.; Munkelwitz, H. R., Water activities, densities, and refractive indices of aqueous sulfates and sodium nitrate droplets of atmospheric importance. *J. Geophys. Res. Atmospheres* **99**, 18801–18808 (1994).
12. Zardini, A. A.; Sjogren, S.; Marcolli, C.; Krieger, U. K.; Gysel, M.; Weingartner, E.; Baltensperger, U.; Peter, T., A combined particle trap/HTDMA hygroscopicity study of mixed inorganic/organic aerosol particles. *Atmospheric Chem. Phys.* **8**, 5589–5601 (2008).
13. Chylek, P., Partial-wave resonances and the ripple structure in the Mie normalized extinction cross section. *JOSA* **66**, 285–287 (1976).
14. Bodem, C. R.; Lampton, L. M.; Miller, D. P.; Tarka, E. F.; Everett, E. D., Endobronchial pH: relevance to aminoglycoside activity in gram-negative bacillary pneumonia. *Am. Rev. Respir. Dis.* **127**, 39–41 (1983).
15. Choudhury, D.; Tanner, M. G.; McAughtrie, S.; Yu, F.; Mills, B.; Choudhary, T. R.; Seth, S.; Craven, T. H.; Stone, J. M.; Mati, I. K.; Campbell, C. J.; Bradley, M.; Williams, C. K. I.; Dhaliwal, K.; Birks, T. A.; Thomson, R. R., Endoscopic sensing of alveolar pH. *Biomed. Opt. Express* **8**, 243–259 (2017).
16. Holma, B., Effects of inhaled acids on airway mucus and its consequences for health. *Environ. Heal. Perspectives* **79**, 109–113 (1989).
17. Kim, D.; Liao, J.; Hanrahan, J. W., The buffer capacity of airway epithelial secretions. *Front. Physiol.* **5**, 188 (2014).
18. Carslaw, K. S.; Clegg, S. L.; Brimblecombe, P., A thermodynamic model of the system HCl-HNO_3-H_2SO_4-H_2O, including solubilities of HBr, from <200 to 328 K. *J. Phys. Chem.* **99**, 11557–11574 (1995).
19. Luo, B.; Carslaw, K. S.; Peter, T.; Clegg, S. L., Vapour pressures of $H_2SO_4/HNO_3/HCl/HBr/H_2O$ solutions to low stratospheric temperatures. *Geophys. Res. Lett.* **22**, 247–250 (1995).

20. Clegg, S. L.; Brimblecombe, P.; Wexler, A. S., Thermodynamic model of the system H^+-NH_4^+-SO_4^{2-}-NO_3-H_2O at tropospheric temperatures. *J. Phys. Chem. A* **102**, 2137–2154 (1998).
21. Chan, C. K.; Liang, Z.; Zheng, J.; Clegg, S. L.; Brimblecombe, P., Thermodynamic properties of aqueous aerosols to high supersaturation: I—measurements of water activity of the system Na^+- Cl^--NO_3^--SO_4^{2-}-H_2O at $\sim$ 298.15 K. *Aerosol Sci. Technol.* **27**, 324–344 (1997).
22. Banerjee, P.; Bagchi, B., Ions' motion in water. *J. Chem. Phys.* **150**, 190901 (2019).
23. Staunton, S., Diffusion processes in *Encyclopedia of Soil Science*, ed. Chesworth, W. (Springer Netherlands), pp. 185–191 (2008).
24. Péraud, J.-P.; Nonaka, A.; Chaudhri, A.; Bell, J. B.; Donev, A.; Garcia, A. L., Low mach number fluctuating hydrodynamics for electrolytes. *Phys. Rev. Fluids* **1**, 074103 (2016).
25. Gillespie, D.; Nonner, W.; Eisenberg, R. S., Coupling Poisson-Nernst-Planck and density functional theory to calculate ion flux. *J. Phys. Condens. Matter* **14**, 12129–12145 (2002).
26. Pruppacher, H.; Klett, J., Microstructure of Atmospheric Clouds and Precipitation in *Microphysics of Clouds and Precipitation*. (Springer, Dordrecht, Dordrecht), 2 edition, pp. 10–73 (2010).
27. Lienhard, D. M.; Huisman, A. J.; Bones, D. L.; Te, Y. F.; Luo, B. P.; Krieger, U. K.; Reid, J. P., Retrieving the translational diffusion coefficient of water from experiments on single levitated aerosol droplets. *Phys. Chem. Chem. Phys.* **16**, 16677–16683 (2014).
28. Balachandar, S.; Zaleski, S.; Soldati, A.; Ahmadi, G.; Bourouiba, L., Host-to-host airborne transmission as a multiphase flow problem for science-based social distance guidelines. *Int. J. Multiph. Flow* **132**, 103439 (2020).
29. Rosti, M.; Olivieri, S.; Cavaiola, M.; Seminara, A.; Mazzino, A., Fluid dynamics of covid-19 airborne infection suggests urgent data for a scientific design of social distancing. *Sci. Reports* **10**, 1–9 (2020).
30. Wang, J.; Alipour, M.; Soligo, G.; Roccon, A.; De Paoli, M.; Picano, F.; Soldati, A., Short-range exposure to airborne virus transmission and current guidelines. *Proc. Natl. Acad. Sci.* **118**, e2105279118 (2021).
31. Berry, E., Relative humidity of expired air. *Am. Phys. Educ. Rev.* **19**, 452–454 (1914).
32. Berg, H. C., *Random Walks in Biology*. (Princeton University Press, Princeton NJ), (1993).
33. Shao, Y.; Ramachandran, S.; Arnold, S.; Ramachandran, G., Turbulent eddy diffusion models in exposure assessment - Determination of the eddy diffusion coefficient. *J. Occup. Environ. Hyg.* **14**, 195–206 (2017).
34. Murphy, D. M.; Koop, T., Review of the vapour pressures of ice and supercooled water for atmospheric applications. *Q. J. Royal Meteorol. Soc.* **131**, 1539–1565 (2005).
35. Nazaroff, W. W.; Weschler, C. J., Indoor acids and bases. *Indoor Air* **30**, 559–644 (2020).
36. Nishihama, Y.; Jung, C. R.; Nakayama, S. F.; Tamura, K.; Isobe, T.; Michikawa, T.; Iwai-Shimada, M.; Kobayashi, Y.; Sekiyama, M.; Taniguchi, Y.; Yamazaki, S., Indoor air quality of 5,000 households and its determinants. Part A: Particulate matter (PM2.5 and PM10–2.5) concentrations in the Japan Environment and Children's Study. *Environ. Res.* **198**, 111196 (2021).
37. Pöhlker, M. L.; Krüger, O. O.; Förster, J.-D.; Berkemeier, T.; Elbert, W.; Fröhlich-Nowoisky, J.; Pöschl, U.; Pöhlker, C.; Bagheri, G.; Bodenschatz, E.; Huffman, J. A.; Scheithauer, S.; Mikhailov, E., Respiratory aerosols and droplets in the transmission of infectious diseases. *arXiv preprint arXiv:2103.01188* (2021).
38. Seinfeld, J. H.; Pandis, S. N., *Atmospheric chemistry and physics: from air pollution to climate change*. (J. Wiley, Hoboken, N.J), 6th edition, (2006).
39. Harper, G. J., Airborne micro-organisms: survival tests with four viruses. *Epidemiol. & Infect.* **59**, 479–486 (1961).
40. Lin, K.; Schulte, C. R.; Marr, L. C., Survival of MS2 and Φ6 viruses in droplets as a function of relative humidity, pH, and salt, protein, and surfactant concentrations. *PLOS ONE* **15**, e0243505 (2020).
41. Vaughan, J.; Ngamtrakulpanit, L.; Pajewski, T. N.; Turner, R.; Nguyen, T. A.; Smith, A.; Urban, P.; Hom, S.; Gaston, B.; Hunt, J., Exhaled breath condensate pH is a robust and reproducible assay of airway acidity. *Eur. Respir. J.* **22**, 889–894 (2003).

42. Chellali, M. R.; Balogh, Z.; Bouchikhaoui, H.; Schlesiger, R.; Stender, P.; Zheng, L.; Schmitz, G., Triple junction transport and the impact of grain boundary width in nanocrystalline cu. *Nano Lett.* **12**, 3448–3454 (2012).
43. Kormuth, K. A.; Lin, K.; Prussin II, A. J.; Vejerano, E. P.; Tiwari, A. J.; Cox, S. S.; Myerburg, M. M.; Lakdawala, S. S.; Marr, L. C., Influenza virus infectivity is retained in aerosols and droplets independent of relative humidity. *J. Infect. Dis.* **218**, 739–747 (2018).
44. Schuit, M.; Gardner, S.; Wood, S.; Bower, K.; Williams, G.; Freeburger, D.; Dabisch, P., The influence of simulated sunlight on the inactivation of influenza virus in aerosols. *J. Infect. Dis.* **221**, 372—378 (2020).
45. Bourgeois, J. F.; Barja, F., The history of vinegar and of its acetification systems. *Arch. des Sci.* **62**, 147–160 (2009).
46. Huang, Y., The SARS epidemic and its aftermath in China: a political perspective in *Learning from SARS - Preparing for the Next Disease Outbreak: Workshop Summary.* (Institute of Medicine, The National Academies Press, Washington DC), pp. 116 – 136 (2004).
47. Greatorex, J. S.; Page, R. F.; Curran, M. D.; Digard, P.; Enstone, J. E.; Wreghitt, T.; Powell, P. P.; Sexton, D. W.; Vivancos, R.; Nguyen-Van-Tam, J. S., Effectiveness of common household cleaning agents in reducing the viability of human influenza A/H1N1. *PLoS ONE* **5**, e8987 (2010).
48. Pagani, I.; Ghezzi, S.; Clementi, M.; Poli, G.; Bussi, M.; Pianta, L.; Trimarchi, M.; Vicenzi, E.; Pagani, I., https://www.biorxiv.org/content/10.1101/2020.07.08.193193v2.abstract: Vinegar and Its Active Component Acetic Acid Inhibit SARS-CoV-2 Infection In Vitro and Ex Vivo. *bioRxiv : preprint server for biology* p. 2020.07.08.193193 (2020).
49. Zardini, A. A.; Krieger, U. K.; Marcolli, C., White light Mie resonance spectroscopy used to measure very low vapor pressures of substances in aqueous solution aerosol particles. *Opt. Express* **14**, 6951 (2006).
50. Zardini, A. A.; Krieger, U. K., Evaporation kinetics of a non-spherical, levitated aerosol particle using optical resonance spectroscopy for precision sizing. *Opt. Express* **17**, 4659–4669 (2009).
51. Walker, J. S.; Archer, J.; Gregson, F. K.; Michel, S. E.; Bzdek, B. R.; Reid, J. P., Accurate representations of the microphysical processes occurring during the transport of exhaled aerosols and droplets. *ACS Cent. Sci.* **7**, 200–209 (2021).
52. Ciobanu, V. G.; Marcolli, C.; Krieger, U. K.; Weers, U.; Peter, T., Liquid-liquid Phase separation in mixed organic/inorganic aerosol particles. *J. Phys. Chem. A* **113**, 10966–10978 (2009).
53. Kumar, A.; Terakosolphan, W.; Hassoun, M.; Vandera, K. K.; Novicky, A.; Harvey, R.; Royall, P. G.; Bicer, E. M.; Eriksson, J.; Edwards, K.; Valkenborg, D.; Nelissen, I.; Hassall, D.; Mudway, I. S.; Forbes, B., A biocompatible synthetic lung fluid based on human respiratory tract lining fluid composition. *Pharm. Res.* **34**, 2454–2465 (2017).
54. Braun, C.; Krieger, U. K., Two-dimensional angular light-scattering in aqueous NaCl single aerosol particles during deliquescence and efflorescence. *Opt. Express* **8**, 314–321 (2001).
55. Dabisch, P.; Schuit, M.; Herzog, A.; Beck, K.; Wood, S.; Krause, M.; Miller, D.; Weaver, W.; Freeburger, D.; Hooper, I.; Green, B.; Williams, G.; Holland, B.; Bohannon, J.; Wahl, V.; Yolitz, J.; Hevey, M.; Ratnesar-Shumate, S., The influence of temperature, humidity, and simulated sunlight on the infectivity of SARS-CoV-2 in aerosols. *Aerosol Sci. Technol.* **55**, 142–153 (2021).
56. Hemmes, J. H.; Winkler, K. C.; Kool, S. M., Virus survival as a seasonal factor in influenza and poliomyelitis. *Nature* **188**, 430–431 (1960).
57. Schaffer, F. L.; Soergel, M. E.; Straube, D. C., Survival of airborne influenza virus: Effects of propagating host, relative humidity, and composition of spray fluids. *Arch. Virol.* **51**, 263–273 (1976).
58. van Doremalen, N.; Bushmaker, T.; Morris, D. H.; Holbrook, M. G.; Gamble, A.; Williamson, B. N.; Tamin, A.; Harcourt, J. L.; Thornburg, N. J.; Gerber, S. I.; Lloyd-Smith, J. O.; de Wit, E.; Munster, V. J., Aerosol and surface stability of SARS-CoV-2 as compared with SARS-CoV-1. *New Engl. J. Medicine* **382**, 1564–1567 (2020).
59. Schuit, M.; Ratnesar-Shumate, S.; Yolitz, J.; Williams, G.; Weaver, W.; Green, B.; Miller, D.; Krause, M.; Beck, K.; Wood, S.; Holland, B.; Bohannon, J.; Freeburger, D.; Hooper, I.; Biryukov, J.; Altamura, L. A.; Wahl, V.; Hevey, M.; Dabisch, P., Airborne SARS-CoV-2 is rapidly inactivated by simulated sunlight. *J. Infect. Dis.* **222**, 564–571 (2020).

60. Bandura, A. V.; Lvov, S. N., The ionization constant of water over wide ranges of temperature and density. *J. Phys. Chem. Ref. Data* **35**, 15–30 (2006).
61. Renard, J. J.; Calidonna, S. E.; Henley, M. V., Fate of ammonia in the atmosphere - A review for applicability to hazardous releases. *J. Hazard. Mater.* **108**, 29–60 (2004).
62. Sander, R., Compilation of Henry's law constants (version 4.0) for water as solvent. *Atmospheric Chem. Phys.* **15**, 4399–4981 (2015).
63. Harned, H. S.; Ehlers, R. W., The dissociation constant of acetic acid from 0 to 60° centigrade. *J. Am. Chem. Soc.* **55**, 652–656 (1933).
64. Morse, J. W.; Mackenzie, F. T., *Geochemistry of Sedimentary Carbonates*. (Amsterdam) Vol. 48, (1990).
65. Woosley, R. J., Evaluation of the temperature dependence of dissociation constants for the marine carbon system using pH and certified reference materials. *Mar. Chem.* **229**, 103914 (2021).
66. Pinho, S. P.; Macedo, E. A., Solubility of NaCl, NaBr, and KCl in water, methanol, ethanol, and their mixed solvents. *J. Chem. Eng. Data* **50**, 29–32 (2005).
67. Roberge, P. R., *Corrosion Engineering - Principles and Practice*. (McGraw-Hill), (2008).
68. Frank, M. J. W.; Kuipers, J. A. M.; Van Swaaij, W. P. M., Diffusion Coefficients and Viscosities of CO_2 + H_2O, CO_2 + CH_3OH, NH_3 + H_2O, and NH_3 + CH_3OH Liquid Mixtures. *J. Chem. Eng. Data* **41**, 297–302 (1996).
69. Kreft, J. U.; Picioreanu, C.; Wimpenny, J. W.; Van Loosdrecht, M. C., Individual-based modelling of biofilms. *Microbiology* **147**, 2897–2912 (2001).
70. Dryahina, K.; Pospíšilová, V.; Sovová, K.; Shestivska, V.; Kubišta, J.; Spesyvyi, A.; Pehal, F.; Turzíková, J.; Votruba, J.; Španěl, P., Exhaled breath concentrations of acetic acid vapour in gastro-esophageal reflux disease. *J. Breath Res.* **8**, 037109 (2014).
71. Smith, D.; Sovová, K.; Dryahina, K.; Doušová, T.; Dřevínek, P.; Španěl, P., Breath concentration of acetic acid vapour is elevated in patients with cystic fibrosis. *J. Breath Res.* **10**, 021002 (2016).
72. Ejaimi, G.; Saeed, S., An introduction to airway assessment and management (concise airway anatomy and pathophysiology). *Annals Int. medical Dental Res.* **3**, 1–7 (2016).